

3. COMPOSITION, PETROGRAPHY, AND MINERAL CHEMISTRY OF ODP SITE 1224 EOCENE FERROBASALTS (LEG 200; NORTH PACIFIC OCEAN)¹

Michele Lustrino^{2,3}

ABSTRACT

The ~46-m.y.-old igneous basement cored during Leg 200 in the North Pacific represents one of the few cross sections of Pacific oceanic crust with a total penetration into basalt of >100 m. The rocks, emplaced during the Eocene at a fast-spreading rate (~14 cm/yr; full rate) are strongly differentiated tholeiitic basalts (ferrobasalts) with 7–4.5 wt% MgO, relatively high TiO₂ (2–3.5 wt%), and total iron as Fe₂O₃ (9.1–16.8 wt%). The differentiated character of these lavas is related to unusually large amounts of crystallization differentiation of plagioclase, clinopyroxene, and olivine.

The lithostratigraphy of the basement (cored to ~170 meters below seafloor) is divided into three units. The deepest unit (lithologic Unit 3), is a succession of lava flows of no more than a few meters thickness each. The intermediate unit (lithologic Unit 2) is represented by intermixed thin flows and pillows, whereas the shallowest unit (lithologic Unit 1), comprises two massive flows. The rocks range from aphyric to sparsely clinopyroxene-plagioclase-phyric (phenocryst content = <3 vol%) and from holocrystalline to hypohyaline. Chilled margins of pillow fragments show holohyaline to sparsely vitrophyric textures.

Site 1224 oxide minerals present a type of alteration not previously seen, where titanomagnetite is only partially destroyed and the pure magnetite component is partially removed from the mineral, leaving, in the most extreme case, a nearly pure ulvöspinel residuum. As a result of this dissolution, iron, mainly in the oxidized state, is added to the

¹Lustrino, M., 2006. Composition, petrography, and mineral chemistry of ODP Site 1224 Eocene ferrobasalts (Leg 200; North Pacific Ocean). *In* Kasahara, J., Stephen, R.A., Acton, G.D., and Frey, F.A. (Eds.), *Proc. ODP, Sci. Results*, 200, 1–36 [Online]. Available from World Wide Web: <http://www-odp.tamu.edu/publications/200_SR/VOLUME/CHAPTERS/008.PDF>. [Cited YYYY-MM-DD]

²Dipartimento di Scienze della Terra, Università degli Studi di Roma La Sapienza, Piazzale Aldo Moro 5, 00185 Rome, Italy.

michele.lustrino@uniroma1.it

³Istituto di Geologia Ambientale e Geoingegneria, CNR, Piazzale Aldo Moro 5, 00185 Rome, Italy.

circulating solvent fluids. This means that a considerable metal source can result from low-temperature reactions throughout the upper ocean crust.

The coarsest-grained lithologic Unit 1 rocks have interstitial myrmekitic intergrowths of quartz and sodic plagioclase ($\sim\text{An}_{12}$), roughly similar in mineralogy and bulk composition to tonalite/trondhjemite veinlets in abyssal gabbros from the southwest Indian Ocean and Hess Deep, eastern equatorial Pacific. Based on idiomorphic relationships and projections into the simplified Q-Ab-Or-H₂O granite ternary system, the myrmekitic intergrowths formed at the same time as, or just after, the oxide minerals coprecipitated and at low water vapor pressure (~ 0.5 kbar). Their compositions correspond to SiO₂-oligoclase intergrowths that are considerably less potassic than dacitic glasses that erupt, although rarely, along the East Pacific Rise or that have been produced experimentally by partial melting of gabbro. Based on the crystallization history and comparison to experimental data, the original interstitial siliceous liquids resulted from late-stage immiscible separation of siliceous and iron-rich liquids. The rare andesitic lavas found along the East Pacific Rise may be hybrid rocks formed by mixing of these immiscible siliceous melts with basaltic magma.

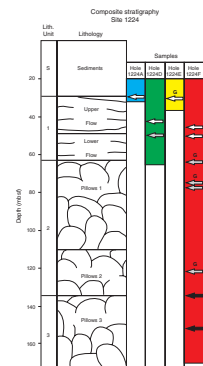
INTRODUCTION

Six holes were drilled at Site 1224, but only four recovered volcanic basement (Fig. F1): Hole 1224A (total depth [TD] = 32.2 meters below seafloor (mbsf); recovery = 5.2%), 1224D (TD = 64.7 mbsf; recovery = 46.7%), 1224E (TD = 36.7 mbsf; recovery = 51.9%), and 1224F (TD = 174.5 mbsf; recovery = 25.7%).

The basement consists of two massive basaltic flows overlying thinner flows and pillow fragments. In general, the cooling unit boundaries of pillows and flows are distinguished by the presence of glass or reductions in grain size. The basalts vary texturally from aphyric to very slightly porphyritic, with very rare plagioclase and clinopyroxene phenocrysts (<3 vol%) occurring in a few samples. The rarity of phenocrysts is typical of basalts from the East Pacific Rise (EPR) and contrast with basalts from more slowly spreading ridges (Bryan, 1983; Hékinian and Morel, 1980; Natland, 1980, 1991; Pan and Batiza, 2002); it has been attributed to the filtering action of the cumulus net of minerals in the column of lower crust that lies directly beneath the steady-state axial magma lens beneath the active portion of the EPR (Natland and Dick, 1996). In basalts from Site 1224, the grain size of groundmass phases is variable, depending on the distance from cooling unit boundaries, but it is generally very fine (<1 mm) except in the coarser interior portions of the two thick flows, which are fine to medium grained (~ 2 mm).

Except for the innermost portion of the massive flows, most of the rocks cored have been altered. Secondary minerals are mostly clays, but Fe-Ti oxyhydroxides, vein sulfides, and carbonates also occur, mostly along cracks and in small cavities. Some basalts experienced marked oxidative alteration that produced striking alteration halos adjacent to fractures (Paul et al., 2006). Nevertheless, Paul et al. (2006) emphasize that Site 1224 basalts are surprisingly unaltered despite their age, perhaps because the igneous basement is capped by massive flows (Fig. F1) that inhibited seawater-basalt interaction.

F1. Lithologic summary, p. 19.



MACROSCOPIC DESCRIPTION OF SAMPLES

On the basis of macroscopic description and geophysical data, the basement section has been divided into three main lithologic units (Stephen, Kasahara, Acton, et al., 2003).

Lithologic Unit 1 (~28–63 mbsf) (Fig. F1) comprises massive basaltic flows with estimated thicknesses of ~35 m and recovery of ~53%. The color of the Unit 1 basalts is dark gray and the grain size is fine, with some gradation to slightly coarser grains toward the middle of the flows. Vesicles are rare and generally <1 cm in diameter with a circular shape. This unit composes the top of basement in Holes 1224A, 1224D, 1224E, and 1224F. The base of this unit probably coincides with a zone characterized by a density and porosity gradient at ~63 mbsf (Stephen, Kasahara, Acton, et al., 2003). Two flows have been identified in this unit on the basis of geochemistry (Lustrino et al., 2004); the contact between these two subunits may be identified as a relatively altered level particularly evident in Hole 1224D at ~48–50 mbsf. Additional evidence for two flows in Unit 1 are chilled margins and degassing structures (probably gas pipes) at the top of the lower flow (interval 200-1224D-4R-1, 11.5–21.5 cm). At least some of the vertical fractures may be related to cooling of the flow; most fractures in the basalts of Holes 1224D and 1224F are filled by clay minerals, oxyhydroxides, carbonate, and pyrite. Unit 1 samples from Hole 1224F show higher content of secondary minerals compared to Unit 1 in Hole 1224D.

Lithologic Unit 2 (~63–133 mbsf) (Fig. F1) comprises thin flows and pillow fragments that were cored in Hole 1224F only, with an estimated total thickness of ~71 m and relatively low recovery (~15%), which reflects the abundant fractures in thin flows and pillow fragments that are poorly cemented by carbonate. Most of the basaltic fragments show brownish alteration halos propagating from fractures, in many cases filled by iron oxyhydroxides. At least a dozen pillow lavas and thin flows have been identified in this unit on the basis of chilled margins (Stephen, Kasahara, Acton, et al., 2003). Two hyaloclastite breccias with volcanic glass partially altered to palagonite are cemented by carbonate material and zeolites.

Lithologic Unit 3 (~133–162 mbsf) (Fig. F1) comprises medium thickness flows alternating with thin flows and pillow lavas. These lithologies are found only in Hole 1224F at a recovery of ~21%. Many macroscopic features of this unit (e.g., relatively coarse grained flows, alteration halos, inclined fracture network, and intercalation of finer-grained basalts with pillow fragments) are common to the first two units.

Petrography

The petrographic characteristics of Site 1224 basalts are reported in Stephen, Kasahara, Acton, et al. (2003). The most important features observed in thin sections are summarized here. The dominant minerals are plagioclase, clinopyroxene, and opaque minerals (both ilmenite-hematite and ulvöspinel-magnetite solid solutions), with rare olivine that is almost always iddingsitized. The presence of pigeonite, observed on the basis of onboard petrographic investigation and identified on the basis of pseudouniaxial character (interval 200-1224D-3R-1, 50–53 cm; $2V\gamma \sim 5^\circ$) has not been confirmed by electron probe microanalysis

(EPM). Anhedral groundmass quartz is rare and occurs only in the most evolved samples.

Both massive and thin flows are nearly aphyric; only very few intervals are characterized by sparsely phyric lithologies (phenocryst content is always <3 vol%). Granularity ranges from holocrystalline (<10% glass) to hypocrySTALLINE (~10%–50% glass), and the texture is isotropic, intergranular, and only rarely subophitic or intersertal. The average dimension of groundmass minerals ranges from very fine (<0.5 mm) to fine (~0.5–1 mm). Considering the age of the samples, the preservation of the basalts is surprising, with a general content of clay minerals (mostly replacing devitrified glass) <5 vol% and never exceeding 20 vol% (e.g., Paul et al., 2006).

Pillow fragments are generally aphyric, ranging from hypocrySTALLINE to hypohyaline (~50–90% glass), with isotropic texture characterized by hyalopilitic and intersertal relationships among groundmass phases.

Hole 1224A

The upper chilled margin in contact with the overlying sediment is >90% brownish to yellow-orange volcanic glass; the change in color is a consequence of palagonitization. The microcrystalline portion of the chilled margin is composed of plagioclase, clinopyroxene, and rare iddingsite pseudomorphs of olivine. Vesicles are <1 vol% and partially filled by clay minerals.

The extremely rare phenocrysts in the basalt are euhedral tabular plagioclase, with a maximum dimension of ~1.2 mm, associated with euhedral prismatic to pseudo-octagonal clinopyroxene with a maximum dimension of ~3 mm. The intersertal to intergranular and rarely subophitic groundmass is made up of the same minerals, plus opaque minerals with an average dimension of 0.1–0.2 mm. Groundmass plagioclase is often skeletal, whereas groundmass clinopyroxene is anhedral; opaque minerals are either acicular or equant. Interstitial brownish devitrified volcanic glass is nearly ubiquitous (~10 vol%) and is associated with plagioclase spherulites. Millimeter-size segregation vesicles are common as dark portions with circular shapes or as irregular pods composed of acicular to skeletal plagioclase, anhedral equant clinopyroxene, acicular opaques, and secondary clay minerals.

Hole 1224D

The mineralogy in Hole 1224D is similar to that of Hole 1224A basalts, that is, rare plagioclase and clinopyroxene phenocrysts (present also as glomerules) and plagioclase, clinopyroxene, and opaque minerals as groundmass phases with an average dimension <0.5 mm. Groundmass plagioclase is commonly present as open spherulites composed of radial crystalites and interstitial clinopyroxene. The texture is holocrystalline, hypidiomorph, and equigranular. The transition zone between the upper and lower flow of lithostratigraphic Unit 1 (Fig. F1) is an alteration zone characterized by highly altered groundmass phases. The main difference between the transition zone and the flows at top and bottom is the relative abundance of segregation vesicles, which may reach as much as 25 vol% in thin section; some vesicles contain small spherical sulfides. The abundance of subspherical cavities generally decreases with increasing depth from ~6 to ~1 vol%. They range from empty to partially or totally filled by clay minerals and/or

plagioclase-clinopyroxene microlitic overgrowth, carbonate, and sulfide.

Filamentous structures in calcite-filled subspherical cavities at 51 mbsf resemble fungal hyphae (Schumann et al., 2004). These hyphae were found within sections perpendicular to the elongation axis of carbonate-filled tubular pores of basalt. These pores have a diameter ranging from ~0.5 to ~3 mm, and the filling media is calcite and aragonite. The net of fungal hyphae completely fills the whole pore space from the basalt/carbonate boundary toward the center of the pores. The cross-section dimension of these hyphae is ~5–10 μm and their length ranges from ~50 μm to several hundred micrometers; therefore, the cell septa of the hyphae are clearly visible. The number of hyphae ranges from tens to hundreds in a pore. Semiquantitative chemical analyses of the etched hyphae show a chemical composition different from the surrounding carbonate matrix. The mineral growth and small open space between the fungi and matrix indicates endolithic fungal growth after the carbonate filling. The presence of euhedral columnar crystals of pyrite in these cavities are evidence of anaerobic conditions (relatively low oxygen fugacity). According to Schumann et al. (2004), this is the first finding of eukaryotic life signs within relatively unaltered deep ocean basaltic rocks.

The top of the lower unit of this hole shows a hypohyaline border (interval 200-1224D-3R-3, 45–48 cm) and structures that may be gas pipe conduits (interval 200-1224D-4R-1, 15–17 cm) with widths varying from ~0.5 to ~5 mm and composed of the same paragenesis of groundmass but with coarser size; some of these conduits are filled by spathic carbonate.

Hole 1224E

Two-thirds of the studied samples are hyaloclastitic breccia with rounded to subrectangular yellowish to pale brownish glass fragments, from ~0.5 to ~3 cm in diameter, cemented by micritic carbonate. Only near the contact with the glass does the carbonate become spathic, with an average crystal dimension of ~0.3 mm. Often, a rim of relatively coarse grained zeolites develops between the glass fragment and carbonate cement. In some cases, the glass is totally replaced by orange palagonite, whereas in other cases the alteration is confined only to the outer rim of the shards. These are generally characterized by rare subhedral plagioclase, clinopyroxene, and iddingsitized olivine microcrysts.

The analyzed aphyric holocrystalline basalt has a texture and mineral paragenesis typical of basalts from the other holes, with <1% of plagioclase phenocrysts and hypidiomorph texture.

Hole 1224F

Hole 1224F is the only hole where all three lithostratigraphic units are present. Unit 1 basalts are similar to previously described Unit 1 basalt from the other holes. These are holocrystalline to hypocrySTALLINE and aphyric with hypidiomorphic isotropic and intergranular groundmass composed of anhedral to subhedral clinopyroxene in intergranular to subophitic relationship with subhedral to euhedral, skeletal to tabular plagioclase, and subhedral opaque minerals. The grain size of groundmass phases varies from ~0.8 to ~0.3 mm. Gabbroic glomerules and phenocrysts are very rare. The peculiarity of Unit 1 basalts in Hole 1224F is the presence of a myrmekitic overgrowth of vermicular Na-rich

plagioclase and quartz, mostly confined to the borders of groundmass or microphenocrysts of plagioclase. Another feature is relatively more alteration compared to Unit 1 basalts from the other holes. Rare iddingsitized olivine has been found in rare pillow fragments.

Unit 2 lithologies are pillow fragments and thin basaltic flows. The pillows show textural variability with holohyaline to hypohyaline, hypocrySTALLINE, and holocrystalline types. These pillow fragments are the only places where microphenocrysts of olivine are not entirely replaced by iddingsite, whereas in the more massive (crystalline) portions of the basaltic flows, only ghosts of olivine are present. The gradation of color of the chilled margin (ranging from yellowish orange to gray toward the inner part) is mostly a result of the palagonitization of the outer rim and the increasing development of plagioclase and clinopyroxene microlites toward the core. Two hyaloclastitic breccias, found at ~76 and 129 mbsf, are composed of subrectangular glassy shards, with a major dimension ranging from ~0.5 to ~3 cm, cemented in a carbonate matrix; palagonitic alteration ranges from nearly total to partial (confined to outer rims).

Unit 3 lithologies are medium-thickness flows interbedded with thin flows and pillow fragments. The petrographic features of these rocks closely resemble those observed for Unit 1 basalts with a similar paragenesis and distribution of segregation vesicles. The only differences are the totally aphyric texture, coarser grain size of groundmass phases (average dimension of single grains > 0.5 mm), strongly fractured groundmass phases, higher content of segregation vesicles, low alteration (~2%), and low porosity (~1% cavities).

MINERAL CHEMISTRY

We report compositions of glasses, adjacent spherulitic portions of pillow rims, principal silicate minerals, Fe-Ti oxides, and some alteration products for 13 basalt samples from Site 1224, for a total of >120 analyses. For these analyses, we utilized a Cameca SX 50 electron microprobe at the Istituto di Geologia Ambientale e Geoingegneria of the Dipartimento di Scienze della Terra of the University of Rome La Sapienza (Italy). Setting conditions are 15 kV and 15nA, whereas the electron beam diameter ranges from 5 µm for oxides, pyroxene, olivine, and plagioclase to 20 µm for glass and myrmekitic intergrowth.

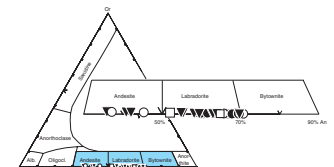
Plagioclase

Plagioclase is the most common groundmass and phenocryst phase. The chemical analyses of plagioclase, An-Ab-Or content, and atomic formulas calculated on the basis of 32 oxygens are reported in Table T1. On the basis of optical properties (e.g., $2V\gamma = \sim 90^\circ$), most of the plagioclase was previously classified as bytownite (Stephen, Kasahara, Acton, et al., 2003), but EMP analyses indicate an andesine-labradorite composition, with anorthite content ranging from An₃₆ to An₇₁ (Fig. F2).

Lithostratigraphic Unit 1 groundmass plagioclase composition is slightly less calcic (An₅₀₋₆₀) than the rare phenocrysts (An₆₃₋₆₇). Such a difference is not observed in lithostratigraphic Unit 2 plagioclase, characterized by phenocrysts and groundmass phases with overlapping An composition higher than Unit 1 plagioclase (An₆₀₋₇₁). On the other hand, lithostratigraphic Unit 3 plagioclase shows An composition over-

T1. Plagioclase, p. 27.

F2. Plagioclase composition, p. 20.



lapping with Unit 1 groundmass plagioclase (An₅₀₋₆₁). With the exception of very few samples, the phenocrysts are unzoned. The few zoned plagioclases show normal zoning with labradoritic core (An₆₄₋₆₆) and andesine rim (An₃₇₋₄₅). Groundmass plagioclase of Units 1 and 3 shows andesine composition (An₃₆₋₄₂).

Clinopyroxene

Clinopyroxene is a major groundmass phase, but it occurs only rarely as a phenocryst, in glomerocrysts, or in gabbroic clots. Chemical analyses of clinopyroxene are reported in Table T2 together with structural formulae calculated on the basis of six oxygens, the Wo-En-Fs molecular weights, Mg# [$Mg\# = Mg/(Mg + Fe^{2+})$] and Cr# [$Cr\# = Cr/(Cr + Al)$]; Fe²⁺ and Fe³⁺ proportion has been calculated using the method of Droop (1987). In the standard Ca-Mg-Fe quadrilateral diagram for pyroxenes (Morimoto et al., 1988), Site 1224 clinopyroxene is augite, albeit showing some compositional variability (Wo₂₈₋₄₂-En₃₆₋₅₈-Fs₁₂₋₃₀) (Fig. F3). The Fe-rich pyroxenes are mostly confined to lithostratigraphic Unit 3; conversely, Unit 2 pyroxenes show the lowest Fe and the highest Ca (Table T2). Rare phenocrysts show very uniform chemical composition. Only one sample shows a weak normal zoning with a core richer in Ca and Mg (Wo₃₉-En₄₂-Fs₁₉) and rim richer in Fe (Wo₃₄-En₄₃-Fs₂₃). Phenocrysts are characterized by the lowest Fe and the highest Ca (Wo₃₄₋₄₀-Fs₁₂₋₁₉) of the data set (Table T2; Fig. F3).

Olivine

Unaltered olivine is extremely rare. Only a single microphenocryst with Fo₇₈ has been analyzed (Sample 200-1224F-11R-2, 13–15 cm; a pillow lava fragment of lithostratigraphic Unit 2) (Table T3). Using olivine-liquid equilibria (Roeder and Emslie, 1970) and assuming a Fe/Mg $K_D = 0.3$, this olivine composition indicates that it crystallized in equilibrium with a moderately evolved liquid (Mg# = ~51). The monticellite molecular content (CaO = 0.35 wt%) is typical of melts equilibrated at relatively low pressures (e.g., Brey and Kohler, 1990).

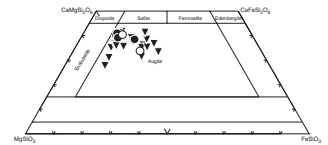
Opaque Minerals

Large and usually skeletal oxide minerals are ubiquitous in the groundmasses of the two flows in lithostratigraphic Unit 1, whereas oxide minerals are much smaller in pillow fragments. These minerals are both rhombohedral (ilmenite-hematite solid solutions) and octahedral (ulvöspinel-magnetite solid solutions). Minerals of the first group are much rarer than those of the second; only a couple of ilmenites were analyzed. EPM data are presented in Table T4 along with structural formulae (calculated on the basis of four oxygens for the spinels and three oxygens for the rhombohedral phases) and Mg#. Ilmenite (Ilm) and ulvöspinel (Usp) molecular content were calculated following Stormer (1983); Fe²⁺ and Fe³⁺ proportion was calculated using the stoichiometric method of Droop (1987).

The spinel phases show some compositional variability (Usp₆₈₋₉₂), whereas the rhombohedral phases are exclusively represented by almost pure ilmenite (Ilm₉₄₋₉₆) (Fig. F4). Titanomagnetite with the highest ulvöspinel content occurs in the lower flow of lithostratigraphic Unit 1

T2. Clinopyroxene, p. 29.

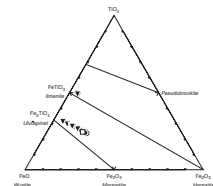
F3. Clinopyroxene composition, p. 21.



T3. Olivine microphenocryst, p. 32.

T4. Opaque minerals, p. 33.

F4. Opaque minerals, p. 22.



(Usp₉₂), whereas spinel in the upper flow has the lowest Ti content (Usp₆₈₋₇₃).

Volcanic Glass

EMP analyses of clear volcanic glass, dark spherulitic glass, and palagonite from pillow rims and hyaloclastites are reported in Table T5; selected major elements vs. the sum of oxides are plotted in Fig. F5. The results show a strong compositional variability, mostly linked to the palagonitization stage of the alteration. The analyzed glass ranges from shards without signs of alteration to shards partially to totally altered in palagonite, belonging both to pillow fragments and hyaloclastitic breccias. Massive basalts contain volcanic glass nearly totally recrystallized to clay minerals.

The range of composition of fresh glass is SiO₂ = 48.7–50.4 wt%, Al₂O₃ = 12.5–14 wt%, TiO₂ = 2.0–2.8 wt%, FeO_{tot} = 12.0–14.2 wt%, MgO = 5.3–7.2 wt%, CaO = 9.8–11.1 wt%, Na₂O = 2.5–3.0 wt%, K₂O = 0.11–0.20 wt%, and P₂O₅ = 0.10–0.33 wt%. The sum of oxides ranges from 97.6 to 99.4 wt% (Fig. F5).

The palagonitized glass shows a much larger range of composition (Table T5; Fig. F5) coupled with lower SiO₂ (40.3–47.9 wt%) and Al₂O₃ (8.4–9.5 wt%), much lower MgO (1.3–3.3 wt%) and CaO (0.5–1.0 wt%), and higher TiO₂ (3.5–3.8 wt%), FeO_{tot} (19.7–23.7 wt%), and K₂O (2.4–3.9 wt%). Na₂O content varies, ranging from values lower than fresh glasses (0.7–1.7 wt%) to much higher values (6.5 wt%) (Table T5). Moreover, palagonitized glass shows MnO and P₂O₅ contents close to the limit of detection (~0.1 wt%) (Table T5). The sum of the oxides is relatively variable but is always lower than unaltered glass (84.6–92.4 wt%), a result presumed to reflect hydration during the palagonitization process.

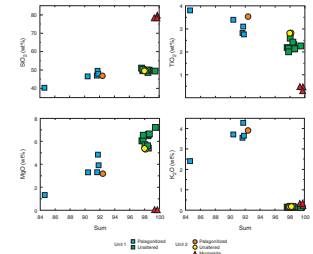
One glassy shard (Sample 200-1224F-6R-1, 29–34 cm, Point 2-1 in Table T5) with optical features of unaltered glass has an intermediate composition. This glass shows SiO₂ (49.6 wt%) and TiO₂ (3.1 wt%) similar to that of unaltered glass but with lower Al₂O₃ (9.3 wt%) and MgO (4.8 wt%). Moreover, this glass shows FeO_{tot} (19.7 wt%), CaO (0.7 wt%), and Na₂O (0.3 wt%) within the range of the palagonitized glasses but with extremely high K₂O (4.3 wt%). This sample probably represents glass at the beginning of the palagonitization stage.

Intergrowth of Quartz and Sodic Plagioclase

Table T6 includes analyses of intergrowths of quartz and alkali feldspar found in Sample 200-1224F-3R-1, 14–16 cm, from lithostratigraphic Unit 1. To obtain an average analysis, the electron beam was defocused to a 20-μm diameter in order to prevent Na volatilization and analyze a large area. The intergrowths developed in interstitial positions between plagioclase laths in the groundmass and as rims on tabular plagioclase (Fig. F6). Shipboard petrologists interpreted this texture as the product of nearly eutectic crystallization of quartz and Na-rich plagioclase (Stephen, Kasahara, Acton, et al., 2003). EMP analyses show evidence of high Al₂O₃ (11.1–12.5 wt%), SiO₂ (78–80 wt%), and Na₂O (5.5–6.2 wt%), whereas CaO, TiO₂, FeO_{tot}, MgO, and K₂O are low (generally <1 wt%) (Fig. F5).

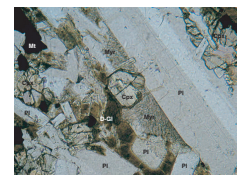
T5. Volcanic glass and palagonite, p. 35.

F5. Volcanic glass content, p. 23.



T6. Myrmekitic intergrowth, p. 36.

F6. Feldspar intergrowth, p. 24.



DISCUSSION

Magmatic Evolution

Site 1224 ferrobasalts are among the most differentiated basalts sampled in the Pacific Ocean crust. They have anomalously high concentrations of incompatible immobile trace elements (e.g., Nb, Zr, Hf, Ta, and Y) (Haraguchi and Ishi, this volume). Lustrino et al. (2004) concluded that Site 1224 basalt formed by variable extents of melting of a typical mid-ocean-ridge basalt (MORB) source, but their highly evolved compositions reflect extensive polybaric fractionation of plagioclase, olivine, and clinopyroxene.

Geothermometry

Using the Beattie (1993) olivine-glass geothermometer, eruptive temperatures were 1147°–1167°C. Using the graphic pyroxene geothermometer of Lindsley and Andersen (1983), pyroxene both near pillow rims that formed at high undercooling and in flow interiors at lesser undercooling began to crystallize from near these temperatures to as low as 1000°C. Titanomagnetite intergrowth with pyroxene began crystallization at ~1050°C, thereby lowering TiO₂ contents in clinopyroxene as crystallization proceeded. At lower temperatures, ilmenite began to crystallize as well. Among the pillow basalts, the clinopyroxenes in each basalt type crystallized within 50°–70°C of the liquid temperatures. In the most slowly cooled interior of the upper flow, the crystallization interval spanned ~130°C, with the most extensively differentiated clinopyroxene occurring in the sample with myrmekitic intergrowths adjacent to plagioclase.

Two-oxide geothermometry (Frost and Lindsley, 1991; Frost et al., 1988) indicates that ilmenite and magnetite crystallized together at ~850°–900°C at an oxygen fugacity about one log unit below the nickel/nickel oxide buffer (ΔNNO). Most titanomagnetite, however, was strongly affected by low-temperature reaction with hydrothermal fluids, losing much of its magnetite (Mt) component to dissolution while retaining ulvöspinel. This may partly have provided the oxidized iron that is in the iron oxyhydroxide veins and adjacent alteration haloes.

Origin of the Quartz-Sodic Plagioclase Intergrowth

Small amounts of felsic rock (e.g., quartz-diorites, tonalites, and trondhjemites) are found in Layer 3 of the oceanic crust and are classically referred to as oceanic plagiogranites (e.g., Thayer, 1977; Aldiss, 1981). Such evolved rocks have been drilled in several Ocean Drilling Program (ODP) sites and in plutonic sections of ophiolites (see Koepke et al., 2004, for a detailed list of occurrences). Many of these plagiogranites show particular microstructures called myrmekites. The term myrmekite designates the “wartlike” appearance of quartz-plagioclase intergrowths seen in thin sections of plutonic rocks (Sederholm, 1897). The term has usually been applied to intergrowths of quartz and sodic plagioclase in rocks with essential K-feldspar, such as granites and gneisses (Barker, 1970). However, reaction rims on calcic plagioclase in basaltic rocks (Pavlov and Karskii, 1949) and main zone gabbroic cumulates of the Bushveld intrusion (Wager and Brown, 1967) have also been termed myrmekite.

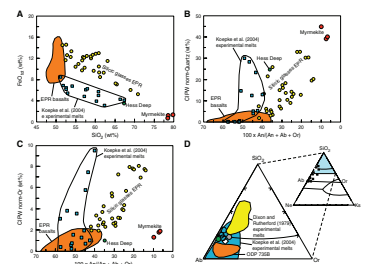
The intergrowths at Site 1224 are similar in bulk composition to the myrmekites in granites (Barker, 1970) and also to dikelets of plagiogranites found in abyssal gabbros from the Southwest Indian Ridge and eastern Pacific (Koepke et al., 2004, and references therein).

The origin of plagiogranites is hotly debated, and three primary models have been proposed: (1) protracted differentiation by crystal fractionation of a MORB parental magma (e.g., Juster et al., 1989; Toplis and Carroll, 1995; Niu et al., 2002), (2) partial melting of oceanic gabbros in high-temperature shear zones (e.g., Cortesogno et al., 2000; Dick et al., 2000; Koepke et al., 2004), and (3) liquid immiscibility (e.g., Dixon and Rutherford, 1979; Natland et al., 1991).

The myrmekitic intergrowths at Site 1224 have higher SiO_2 and lower FeO_{tot} than silicic glasses from the EPR, including a dacite glass bleb found in a ferroandesite dredged from the eastern limb of the 9°N non-transform offset of the East Pacific Rise (Natland, 1991), which is the most siliceous glass thus far analyzed from the ocean basins (Fig. F7A). Moreover, compared to EPR silicic glasses, they have higher Cross, Idings, Pirsson, and Washington (CIPW) normative quartz (Fig. F7B) and much lower normative orthoclase (Fig. F7C). The normative plagioclase composition of the myrmekitic intergrowths is An_{8-10} (Fig. F7B, F7C). The experimental partial melts of cumulate gabbros cored from ODP Legs 176 (Site 735B; Southwest Indian Ridge) and 153 (Mid-Atlantic Ridge Kane Fracture Zone) obtained by Koepke et al. (2004) show compositions very different from those of myrmekites. In particular, Figure F7 shows the lower SiO_2 , lower CIPW normative quartz, and higher FeO_{tot} content of the experimental melts of Koepke et al. (2004) compared to the myrmekitic intergrowths at Site 1224; other differences (not shown) are the higher Al_2O_3 and CaO and lower Na_2O contents of the experimental melts. In the ternary normative diagram representing the granitic portion of petrogeny's residua system (Fig. F7D), two of the three intergrowth compositions from Site 1224 plot nearly at the sideline quartz-albite binary eutectic at a vapor pressure of ~500 atm (0.506 Kbar), consistent with formation at or near the seafloor. The binary eutectic at this point is at ~870°C (Tuttle and Bowen, 1958), a value similar to the temperature estimates for late-stage liquids using coexisting ilmenite and magnetite. The other sample plots toward higher normative quartz. An immiscible dacite globule from dolerite at Deep Sea Drilling Project Site 396, on the eastern flank of the Mid-Atlantic Ridge (Sato, 1979), plots nearby but is somewhat more potassic than the intergrowths. Siliceous glasses segregated experimentally from ferrobalt liquids (Dixon and Rutherford, 1979) do not fall on any of the three-phase cotectic boundaries plotted in Figure F7D but instead have significantly higher normative quartz. The experimental melts of Koepke et al. (2004) show large compositional variation, with values overlapping the composition of the myrmekites of Site 1224 to compositions with much lower quartz (Fig. F7D). Note the overlap between the plagiogranites found in natural samples in Hole 735B and the experimental melts of Koepke et al. (2004), which used Hole 735B gabbros as starting material.

We conclude that the Site 1224 intergrowth compositions are not those of liquids. The projected phase relations suggest instead that they are a cryptocrystalline intergrowth of sodic plagioclase and quartz that precipitated from liquids that plausibly resembled the dacitic natural glass or some of the experimental immiscible siliceous liquids, these liquids being in particular more potassic and more siliceous than the inter-

F7. Myrmekite data, p. 25.



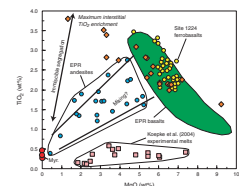
growths. An immiscible origin for the liquids that produced the intergrowths is supported by the lack of a continuum in plagioclase compositions between groundmass plagioclase ($\sim\text{An}_{36}$) and the normative plagioclase compositions (An_{8-10}) of the intergrowths, the sharp boundaries of the intergrowths with adjacent plagioclase, and their coliform shapes where they extend convexly into the mesostasis.

Other mechanisms of formation are possible. Orville (1963) described an ion-exchange reaction between albite ($\text{NaAlSi}_3\text{O}_8$) and a solution with excess CaCl_2 that produced anorthite ($\text{CaAl}_2\text{Si}_2\text{O}_8$) with tiny inclusions of quartz, but he was unable to produce a similar result by reaction between anorthite and a solution with excess NaCl , evidently because of kinetic effects (Barker, 1970, citing a personal communication from P. Orville). Despite this negative result, these experiments do not preclude the possibility that in a more complex natural system, intergrowths of quartz and sodic plagioclase may form by reaction between late-stage magmatic or hydrothermal brines and minerals that crystallized interstitially from highly differentiated, but not necessarily granitic, liquids. Nevertheless, whether it is by direct crystallization differentiation, liquid immiscibility, or metasomatic process, granitic microenvironments clearly develop intersertally even in the coarse-grained flow interiors of parental abyssal tholeiites.

The uniform chemical compositions of least-altered whole rocks show that the intersertal granitic microenvironments remained where they formed; they did not coalesce or concentrate into veins or veinlets in accord with Marsh's (1995) observation that aphyric basaltic liquids lack a mechanism such as buoyancy-driven separation of phenocrysts from liquids to segregate minerals. Only interstitial differentiation occurs in aphyric flows or intrusions, and this does not appreciably affect the bulk compositions of analyzed rocks. A corollary is that formation of veins of tonalite or trondhjemite in abyssal gabbros and even differentiation of basalt types, as exemplified by the short section of basalts cored at Site 1224, requires some additional means of separating crystals from residual liquids. At slow-spreading ridges, the apparent mechanism is expulsion of residual liquids from a crystalline matrix by a combination of compactive and shear deformation (Natland and Dick, 2001), what Bowen (1920) termed "differentiation by deformation." Based on the little-deformed gabbros sampled at Hess Deep in the eastern Pacific, the agency of separation of residual liquids from cumulates beneath fast-spreading ridges is evidently more strongly dominated by compaction than by differential horizontal stress (Natland and Dick, 1996).

Figure F8 summarizes the extended liquid line of descent for abyssal tholeiite magma, as deduced from mineral relations seen at Site 1224 and the gabbro suites from the eastern Pacific. An initial primitive basaltic liquid first crystallizes olivine and plagioclase, with clinopyroxene soon joining the liquidus. This results in a trend of enrichment in FeO_{tot} and TiO_2 until at $\sim 4\%$ – 5% MgO content and 1080° – 1050°C , where titanomagnetite joins plagioclase and clinopyroxene in the crystallization sequence. Iron enrichment persists as crystallization differentiation proceeds, but TiO_2 enrichment is retarded by titanomagnetite crystallization until $\sim 1000^\circ\text{C}$, where two silicate liquids, one very iron rich and the other siliceous, separate immiscibly. The separate liquids each internally continue to differentiate on their own, with ilmenite and titanomagnetite coprecipitating from the more iron rich

F8. EPM analyses, p. 26.



liquid and quartz and sodic plagioclase from the silica-rich liquid to produce dacitic and even truly rhyolitic residua.

Along the EPR, nearly two dozen lavas of generally andesitic composition have been sampled at different places. In hand specimens they are extremely dark rocks, black compared with the gray of basalts, and this is because they are still sufficiently rich in FeO_{tot} and TiO_2 that they crystallize abundant titanomagnetite. They could accurately be termed ferroandesite or even icelandite to distinguish them from the light gray and not nearly as iron-rich calc-alkalic andesite so common in island arcs. If the usual liquid line of descent along the EPR is like that just described and involves late-stage liquid immiscibility, then all andesites from this spreading ridge must be hybrid rocks, mixes between dacitic to rhyodacitic liquids and evolved but nevertheless still common basalt with between 2% and 3% TiO_2 content (double-headed arrows in Fig. F8). The andesites are not simply a continuation of the basaltic liquid line of descent turned abruptly toward lower TiO_2 contents by the onset of crystallization of titanomagnetite and ilmenite. A composite dredge sample having an andesite interior and basalt carapace, obtained from the eastern limb of the 9°N nontransform offset of the EPR, provided clear mineralogical evidence for such mixing (Natland, 1991). Evidence for similar mixing along the Galapagos Spreading Center was presented by Juster et al. (1989).

Alteration Effects

Opaque Minerals Composition

The high ulvöspinel content of the titanomagnetites is a surprise, being quite unlike compositions seen in fresh basalt with a wide range of differentiation dredged from the EPR (Gee and Kent, 1997) or even somewhat altered basalt drilled along the Mid-Atlantic Ridge (Johnson and Melson, 1979). The latter rocks contain cation-deficient titanomaghemite altered after original titanomagnetite. The cation-deficient titanomaghemite, however, differs only slightly from the fresh mineral in its proportion of magnetite to ulvöspinel and does not approach the deficiency in magnetite found in the spinel that we analyzed from Site 1224 (Fig. F4). The near uniformity of unaltered titanomagnetite in fresh basalt representing different stages of differentiation (i.e., from olivine tholeiites to ferrobasalt) clearly stems from the common composition along a liquid line of descent where this mineral joins the liquidus.

With only a pair of adjacent ilmenites analyzed in a single sample from Site 1224, it is not possible to determine if ilmenite composition correlates with titanomagnetite composition. The two grains lie at the ilmenite-rich, hematite-poor end of the spectrum among basalts and dikes and are similar in composition to many ilmenite grains in abyssal gabbros (Dick et al., 2002).

In general, variations in composition of both ilmenite and magnetite result from oxyexsolution, the first stages of which produce lamellae of ilmenite and magnetite (Buddington and Lindsley, 1964). In the ocean crust, this is most often observed in basalts, dikes, or gabbros that were subjected either to high-temperature hydrothermal alteration (e.g., deep-dike rocks from Hess Deep) or to slow subsolidus cooling in the lower crust (gabbros from Hess Deep and the Southwest Indian Ridge). Indeed, during extensive hydrothermal alteration at greenschist or low-grade amphibolite facies temperatures, a common result is for all the

magnetite to disappear (e.g., Shipboard Scientific Party, 1999; Natland, 2002), leaving only relict lamellae of ilmenite and no high-intensity magnetic minerals.

Site 1224 basalt thus presents a type of alteration of oxide minerals not previously seen, in that titanomagnetite is only partially destroyed with the pure magnetite component being partially removed from the mineral, leaving in the extreme a nearly pure ulvöspinel residuum. In effect, the Fe_2O_3 -bearing component of the mineral is systematically and almost entirely removed. Ilmenite may experience a lesser but similar extraction of its Fe_2O_3 -bearing component, hematite. As a result of this dissolution, iron, mainly in the oxidized state, must be added to the circulating solvent fluids, even at the very highest levels of the ocean crust. Evidently it is soon redeposited as iron oxyhydroxides and amorphous iron oxide in vein minerals and alteration haloes. Thus rather than viewing the sources of metals deposited at ridges to lie entirely within deep hydrothermal reaction zones near substantial magma bodies (e.g., Gillis et al., 2001), we must now consider that perhaps a considerable metal source results from low-temperature reactions occurring throughout the porous and fragmented upper ocean crust.

Glass Alteration

Because of hydration (sum of oxides is 84.6%–92.4%), the mobility of elements during formation of palagonite cannot be accurately assessed using absolute differences in composition between glass and its alteration product. When considered in terms of cation proportions on an anhydrous basis, glass altered to palagonite at pillow rims lost CaO and MgO and gained both total iron as FeO_{tot} and K_2O with respect to the nearly immobile oxides, TiO_2 , Al_2O_3 , and SiO_2 . Na_2O was enriched in some palagonites but depleted in others. The iron was probably provided by the same hydrothermal fluids that added iron oxyhydroxides to veins and alteration haloes in crystalline basalt and/or by low-temperature reactions (see previous paragraph). The K-rich composition of palagonite is ultimately derived from high-temperature nonoxidative alteration of abyssal tholeiites to mineral assemblages carrying chlorite and magnesian saponite deep in the section, since neither mineral allows K into its structure. The potassium is consequently released to the circulating hydrothermal fluids, and it later precipitates near the surface during oxidative formation of K- and Fe-smectite. Loss of CaO in palagonite occurred during transformation of glass to such clay minerals very near the seafloor, in a manner possibly analogous to loss of CaO during basalt alteration lower in the crust. The CaO lost in rocks at any depth plausibly contributes to the formation of late-stage veins of calcite and aragonite in these basalts.

Along with analyses of fresh glass, the compositions of black incipient spherulitic material and of orange palagonite replacing glass were obtained from the same thin sections (Table T5). The spherulitic material differs only slightly from fresh glass in having slightly higher MgO or Al_2O_3 and, in two cases, lower Na_2O . Experimental studies and high-resolution microscopy show that spherulites in abyssal tholeiites are usually made up of extremely tiny needles, fibers, or dendrites of silicate minerals (e.g., Kirkpatrick, 1979). The bulk of the material in an individual spherulite must still be glass, and a defocused electron-probe beam will therefore necessarily intersect some combination of glass and, in these rocks, either plagioclase needles or clinopyroxene den-

drites. The small departures in MgO and Al₂O₃ contents of spherulites from the adjacent glass indicate slight differences in proportions of minerals. Low Na₂O contents in two spherulites may indicate that the glass fraction of the spherulite is altered to palagonite.

A zeolite composition reported in Table T6 (Sample 200-1224F-6R-1, 29–34 cm) is Na- and K-rich aluminosilicates resembling phillipsite. This phase, commonly found in palagonitized submarine vitric tuffs, is generally thought to incorporate alkalis, alumina, and silica derived from formation of palagonite. However, since Al₂O₃ and SiO₂ in Site 1224 palagonites behave mostly as immobile oxides, this origin can be ruled out.

CONCLUSIONS

Late-stage in situ or intersertal crystallization in basalts at Site 1224 resulted in iron-rich differentiates and eventual formation of high-SiO₂ immiscible melt that precipitated quartz and sodic plagioclase at temperatures <970°C. In the case of the seafloor basalts of Site 1224, the residual liquids were not mobile; they did not concentrate into veins. Because of degassing, they were probably significantly less hydrous than residual liquids in the gabbro suites. At no stage, for example, did magmatic amphibole crystallize, whereas titanian pargasite is a common, even abundant, mineral in abyssal gabbros (Stakes et al., 1991; Tribuzio et al., 2000; Gillis and Meyer, 2001).

Some titanomagnetite was strongly affected by alteration, actually losing Fe₂O₃ to circulating hydrothermal fluids, which perhaps contributed to the ubiquitous and widespread infilling of fractures and veins with iron oxyhydroxides. This contrasts with the more typical loss of FeO from titanomagnetite in abyssal-tholeiite dikes and gabbros during oxyexsolution in the middle to lower ocean crust. Potassic and iron-rich smectite also precipitated from similar fluids in vein assemblages. Basaltic glass near the top of the section is partly altered to palagonite, which appears to be another consequence of reaction with low-temperature hydrothermal fluids carrying abundant trivalent iron and potassium in solution. The composite alteration assemblage of veins with iron oxyhydroxides and palagonite enriched in iron can be viewed as a consequence of diffuse fluid flux directed upward from deeper and hotter reaction zones in the lower crust, but also outward from and much more slowly than high-temperature vents at the ridge axis, where iron in fluids is generally reduced and sulfides precipitate in chimneys.

ACKNOWLEDGMENTS

I am deeply indebted with Jim Natland (Miami, Florida, USA) for giving me many hints during the writing of this manuscript. In particular, most of the discussion about the origin of myrmekites comes from his ideas. Detailed reviews of Mike R. Perfit (Gainesville, Florida, USA) and Fred Frey (Cambridge, Massachusetts, USA) greatly improved the quality and readability of this paper. Many thanks also to Isabella Premoli Silva (Milan, Italy) and Piera Spadea (Trieste, Italy) for the opportunity to participate in the ODP cruise and Marcello Serracino for his skilled assistance during EMP analyses. I also want to warmly thank Enrica, Bianca, and Laura for their support during the writing of this manuscript.

This research used samples and/or data provided by the Ocean Drilling Program (ODP). ODP is sponsored by the U.S. National Science Foundation (NSF) and participating countries under management of Joint Oceanographic Institutions (JOI), Inc.

REFERENCES

- Aldiss, D.T., 1981. Plagiogranites from the ocean crust and ophiolites. *Nature (London, U. K.)*, 289:577–578. doi:10.1038/289577a0
- Barker, D.S., 1970. Compositions of granophyre, myrmekite, and graphic granite. *Geol. Soc. Am. Bull.*, 81:3339–3350.
- Beattie, P., 1993. Olivine-melt and orthopyroxene-melt equilibria. *Contrib. Mineral. Petrol.*, 115:103–111. doi:10.1007/BF00712982
- Bowen, N.L., 1920. Differentiation by deformation. *Proc. Nat. Acad. Sci.*, 6:159–162.
- Brey, G.P., and Kohler, T. 1990. Geothermobarometry in four-phase lherzolites. II. New thermobarometers, and practical assessment of existing thermobarometers. *J. Petrol.*, 31:1353–1378.
- Bryan, W.B., 1983. Systematics of modal phenocryst assemblages in submarine basalts: petrologic implications. *Contrib. Mineral. Petrol.*, 83:62–74.
- Buddington, A.F., and Lindsley, D.H., 1964. Iron-titanium oxides minerals and synthetic equivalents. *J. Petrol.*, 5:310–357.
- Cortesogno, L., Gaggero, L., and Zanetti, A., 2000. Rare earth and trace elements in igneous and high-temperature metamorphic minerals of oceanic gabbros (MARK area, Mid-Atlantic Ridge). *Contrib. Mineral. Petrol.*, 139:373–393. doi:10.1007/s004100000147
- Dick, H.J.B., Natland, J.H., Alt, J.C., Bach, W., Bideau, D., Gee, J.S., Haggas, S., Hertogen, J.G.H., Hirth, G., Holm, P.M., Ildefonse, B., Iturrino, G.J., John, B.E., Kelley, D.S., Kikawa, E., Kingdon, A., LeRoux, P.J., Maeda, J., Meyer, P.S., Miller, D.J., Naslund, H.R., Niu, Y.-L., Robinson, P.T., Snow, J., Stephen, R.A., Trimby, P.W., Worm, H.-U., and Yoshinobu, A., 2000. A long in situ section of the lower ocean crust: results of ODP Leg 176 drilling at the Southwest Indian Ridge. *Earth Planet. Sci. Lett.*, 179:31–51. doi:10.1016/S0012-821X(00)00102-3
- Dick, H.J.B., Ozawa, K., Meyer, P.S., Niu, Y., Robinson, P.T., Constantin, M., Hebert, R., Maeda, J., Natland, J.H., Hirth, J.G., and Mackie, S.M., 2002. Primary silicate mineral chemistry of a 1.5-km section of very slow spreading lower ocean crust: ODP Hole 735B, Southwest Indian Ridge. In Natland, J.H., Dick, H.J.B., Miller, D.J., and Von Herzen, R.P. (Eds.), *Proc. ODP, Sci. Results*, 176, 1–61 [Online]. Available from World Wide Web: http://www-odp.tamu.edu/publications/176_SR/VOLUME/CHAPTERS/SR176_10.PDF. [Cited 2005-05-22]
- Dixon, S., and Rutherford, M.J., 1979. Plagiogranites as late-stage immiscible liquids in ophiolite and mid-ocean ridge suites: an experimental study. *Earth Planet. Sci. Lett.*, 45:45–60. doi:10.1016/0012-821X(79)90106-7
- Droop, G.T.R., 1987. A general equation for estimating Fe³⁺ concentrations in ferromagnesian silicates and oxides from microprobe analyses, using stoichiometric criteria. *Mineral. Mag.*, 51:431–435.
- Frost, B.R., and Lindsley, D.H., 1991. Occurrence of iron-titanium oxides in igneous rocks. In Lindsley, D.H. (Ed.), *Oxide Minerals: Petrologic and Magnetic Significance*. Mineral. Soc. Am., Rev. Mineral., 25:433–468.
- Frost, B.R., Lindsley, D.H., and Andersen, D.J., 1988. Fe-Ti oxide-silicate equilibria: assemblages with fayalitic olivine. *Am. Mineral.*, 73:727–740.
- Gee, J., and Kent, D.V., 1997. Magnetization of axial lavas from the southern East Pacific Rise (14°–23°S): geochemical controls on magnetic properties. *J. Geophys. Res.*, 102:24873–24886. doi:10.1029/97JB02544
- Gillis, K.M., and Meyer, P.S., 2001. Metasomatism of oceanic gabbros by late stage melts and hydrothermal fluids: evidence from the rare earth element composition of amphiboles. *Geochem., Geophys., Geosys.*, 2(3). doi:10.1029/2000GC000087
- Gillis, K.M., Muehlenbachs, K., Stewart, M., Gleeson, T., and Karson, J., 2001. Fluid flow patterns in fast spreading East Pacific Rise crust exposed at Hess Deep. *J. Geophys. Res.*, 106:26311–26329. doi:10.1029/2000JB000038

- Hékinian, R., and Morel, J.M., 1980. Basement rocks from the East Pacific Rise near 9°N compared with other ocean-floor volcanic provinces. *In* Rosendahl, B.R., Hékinian, R., et al., *Init. Repts. DSDP*, 54: Washington (U.S. Govt. Printing Office), 819–832.
- Johnson, H.P., and Melson, W.G., 1979. Electron microprobe analyses of some titanomagnetite grains from Hole 395A. *In* Melson, W.G., Rabinowitz, P.D., et al., *Init. Repts. DSDP*, 45: Washington (U.S. Govt. Printing Office), 575–579.
- Juster, T.C., Grove, T.L., and Perfit, M.R., 1989. Experimental constraints on the generation of FeTi basalts, andesites, and rhyodacites at the Galapagos Spreading Center, 85°W and 95°W. *J. Geophys. Res.*, 94:9251–9274.
- Kirkpatrick, R.J., 1979. Processes of crystallization in pillow basalts, Hole 396B, DSDP Leg 46. *In* Dmitriev, L., Heirtzler, et al., 1979. *Init. Repts. DSDP*, 46: Washington (U.S. Govt. Printing Office), 271–282.
- Koepke, J., Feig, S.T., Snow, J., and Freise, M., 2004. Petrogenesis of oceanic plagiogranites by partial melting of gabbros: an experimental study. *Contrib. Mineral. Petrol.*, 146:414–432. doi:10.1007/s00410-003-0511-9
- Lindsley, D.H., and Andersen, D.J., 1983. A two-pyroxene thermometer. *J. Geophys. Res.*, 88 (Suppl.):A887–A906.
- Lustrino, M., Costantini, L., and Haraguchi, S., 2004. Polybaric differentiation of ODP 1224 site ferrobasalts (North Pacific Ocean): major, trace elements and Sr-Nd-Pb isotopic constraints. *Int. Geol. Congr., Rep. Sess.*, 32(2):1426. (Abstract)
- Marsh, B.D., 1995. Solidification fronts and magmatic evolution. *Mineral. Mag.*, 60:5–40.
- Morimoto, N., Fabries, J., Ferguson, A., Ginzburg, I.V., Roos, M., Seifert, F.A., Zussman, J., Aoki, K., and Gottardi, G., 1988. Nomenclature of pyroxenes. *Mineral. Petrol.*, 39(1):55–76. doi:10.1007/BF01226262
- Natland, J.H., 1980. Crystal morphologies in basalts dredged and drilled from the East Pacific Rise near 9°N and the Siqueiros Fracture Zone. *In* Rosendahl, B.R., Hékinian, R., et al., *Init. Repts. DSDP*, 54: Washington (U.S. Govt. Printing Office), 605–634.
- Natland, J.H., 1991. Mineralogy and crystallization of oceanic basalts. *In* Floyd, P.A. (Ed.), *Oceanic Basalts*: Glasgow (Blackie), 63–93.
- Natland, J.H., 2002. Magnetic susceptibility as an index of the lithology and composition of gabbros, ODP Leg 176, Hole 735B, Southwest Indian Ridge. *In* Natland, J.H., Dick, H.J.B., Miller, D.J., and Von Herzen, R.P. (Eds.), *Proc. ODP, Sci. Results*, 176, 1–69 [Online]. Available from World Wide Web: http://www-odp.tamu.edu/publications/176_SR/VOLUME/CHAPTERS/SR176_11.PDF. [Cited 2005-05-22]
- Natland, J.H., and Dick, H.J.B., 1996. Melt migration through high-level gabbroic cumulates of the East Pacific Rise at Hess Deep: the origin of magma lenses and the deep crustal structure of fast-spreading ridges. *In* Mével, C., Gillis, K.M., Allan, J.F., and Meyer, P.S. (Eds.), *Proc. ODP, Sci. Results*, 147: College Station, TX (Ocean Drilling Program), 21–58.
- Natland, J.H., and Dick, H.J.B., 2001. Formation of the lower ocean crust and the crystallization of gabbroic cumulates at a very slowly spreading ridge. *J. Volcanol. Geotherm. Res.*, 110:191–233.
- Natland, J.H., Meyer, P.S., Dick, H.J.B., and Bloomer, S.H., 1991. Magmatic oxides and sulfides in gabbroic rocks from Hole 735B and the later development of the liquid line of descent. *In* Von Herzen, R.P., Robinson, P.T., et al., *Proc. ODP, Sci. Results*, 118: College Station, TX (Ocean Drilling Program), 75–111.
- Niu, Y., Gilmore, T., Mackie, S., Greig, A., and Bach, W., 2002. Mineral chemistry, whole-rock compositions, and petrogenesis of Leg 176 gabbros: data and discussion. *In* Natland, J.H., Dick, H.J.B., Miller, D.J., and Von Herzen, R.P. (Eds.), *Proc. ODP, Sci. Results*, 176, 1–60 [Online]. Available from World Wide Web: http://www-odp.tamu.edu/publications/176_SR/VOLUME/CHAPTERS/SR176_08.PDF. [Cited 2005-05-22]

- Orville, P.M., 1963. Alkali ion exchange between vapor and feldspar phases. *Am. J. Sci.*, 251:201–237.
- Pan, Y., and Batiza, R., 2002. Mid-ocean ridge magma chamber processes: constraints from olivine zonation in lavas from the East Pacific Rise at 9°30'N and 10°30'N. *J. Geophys. Res.*, 107:1–13. doi:10.1029/2001JB000435
- Paul, H.J., Gillis, K.M., Coggon, R.M., and Teagle, D.A.H., 2006. ODP Site 1224: a missing link in the investigation of seafloor weathering. *Geochem., Geophys., Geosyst.*, 7(2). doi:10.1029/2005GC001089
- Pavlov, N.V., and Karskii, B.E., 1949. On myrmekite in some basic rocks. *Izv. Akad. Nauk SSSR, Ser. Geol.*, 5:128–136.
- Pedersen, R.B., Malpas, J., and Falloon, T., 1996. Petrology and geochemistry of gabbroic and related rocks from Site 894, Hess Deep. In Mével, C., Gillis, K.M., Allan, J.F., and Meyer, P.S. (Eds.), *Proc. ODP, Sci. Results*, 147: College Station, TX (Ocean Drilling Program), 3–19.
- Roeder, P.L., and Emslie, R.F., 1970. Olivine-liquid equilibrium. *Contrib. Mineral. Petrol.*, 29:275–289. doi:10.1007/BF00371276
- Sato, H., 1979. Segregation vesicles and immiscible liquid droplets in ocean-floor basalt of Hole 396B, IPOD/DSDP Leg 46. In Dmitriev, L., Heirtzler, J., et al, *Init. Repts. DSDP*, 46: Washington (U.S. Govt. Printing Office), 283–297.
- Schumann, G., Manz, W., Reitner, J., and Lustrino, M., 2004. Ancient fungal life in north Pacific Eocene oceanic crust. *Geomicrobiol. J.*, 1:241–246. doi:10.1080/01490450490438748
- Sederholm, J.J., 1897. Über eine archaische Sedimentformation im südwestlichen Finnland und ihre Bedeutung für die Erklärung der Entstehungsweise des Grundgebirges. *Bull. Comm. Geol. Finl.*, 6:1–254.
- Shipboard Scientific Party, 1999. Leg 176 summary. In Dick, H.J.B., Natland, J.H., Miller, D.J., et al., *Proc. ODP, Init. Repts.*, 176, 1–70 [CD-ROM]. Available from: Ocean Drilling Program, Texas A&M University, College Station, TX 77845-9547, U.S.A. [HTML]
- Stakes, D., Mével, C., Cannat, M., and Chaput, T., 1991. Metamorphic stratigraphy of Hole 735B. In Von Herzen, R.P., Robinson, P.T., et al., *Proc. ODP, Sci. Results*, 118: College Station, TX (Ocean Drilling Program), 153–180.
- Stephen, R.A., Kasahara, J., Acton, G.D., et al., 2003. *Proc. ODP, Init. Repts.*, 200 [CD-ROM]. Available from: Ocean Drilling Program, Texas A&M University, College Station TX 77845-9547, USA. [HTML]
- Stormer, J.C., Jr., 1983. The effects of recalculation on estimates of temperature and oxygen fugacity from analyses of multicomponent iron-titanium oxides. *Am. Mineral.*, 68:586–594.
- Thayer, T.P., 1977. Some implications of sheeted dike swarms in ophiolitic complexes. *Geotectonics*, 11:419–426.
- Toplis, M.J., and Carroll, M.R., 1995. An experimental study of the influence of oxygen fugacity on Fe-Ti oxide stability, phase relations, and mineral-melt equilibria in ferrobaltic systems. *J. Petrol.*, 36:1137–1170.
- Tribuzio, R., Tiepolo, M., and Thirlwall, M.F., 2000. Origin of titanian pargasite in gabbroic rocks from the Northern Apennine ophiolites (Italy): insights into the late-magmatic evolution of a MOR-type intrusive sequence. *Earth Planet. Sci. Lett.*, 176:281–293. doi:10.1016/S0012-821X(00)00014-5
- Tuttle, O.F., and Bowen, N.L., 1958. Origin of granite in the light of experimental studies in the system NaAlSi₃O₈-KAlSi₃O₈-SiO₂-H₂O. *Mem.—Geol. Soc. Am.*, 74.
- Wager, L.R., and Brown, G.M., 1967. *Layered Igneous Rocks*: San Francisco (W.H. Freeman).

Figure F1. Lithologic summary of sediments and basalts cored at Site 1224. Arrows = location of investigated thin sections, G = thin sections with glass. All of the drilling activity occurred within a ~20 m × 20 m area.

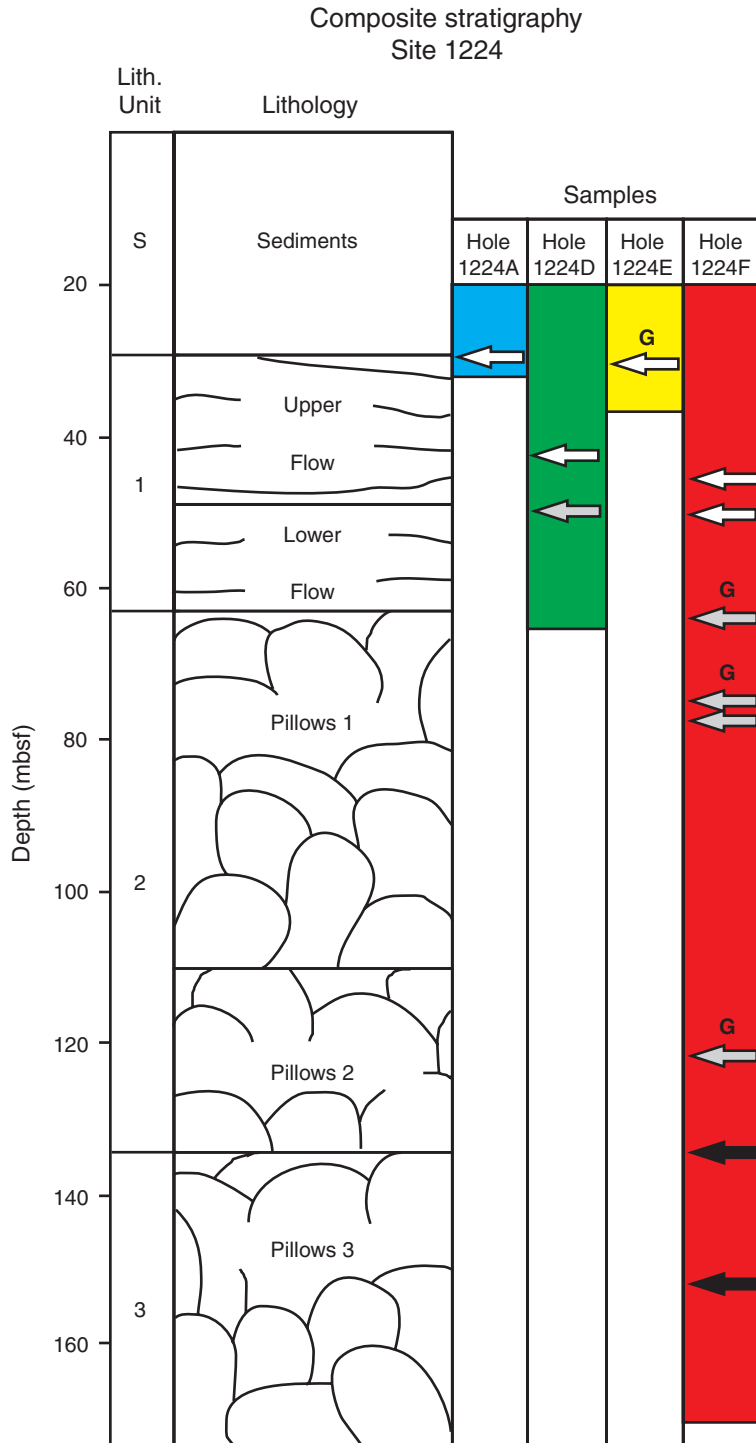


Figure F2. Plagioclase composition of Site 1224 ferrobasalts plotted in the conventional Ab-An-Or classification scheme. Solid triangles = groundmass phases, open circles = phenocryst rims, solid circles = phenocryst cores.

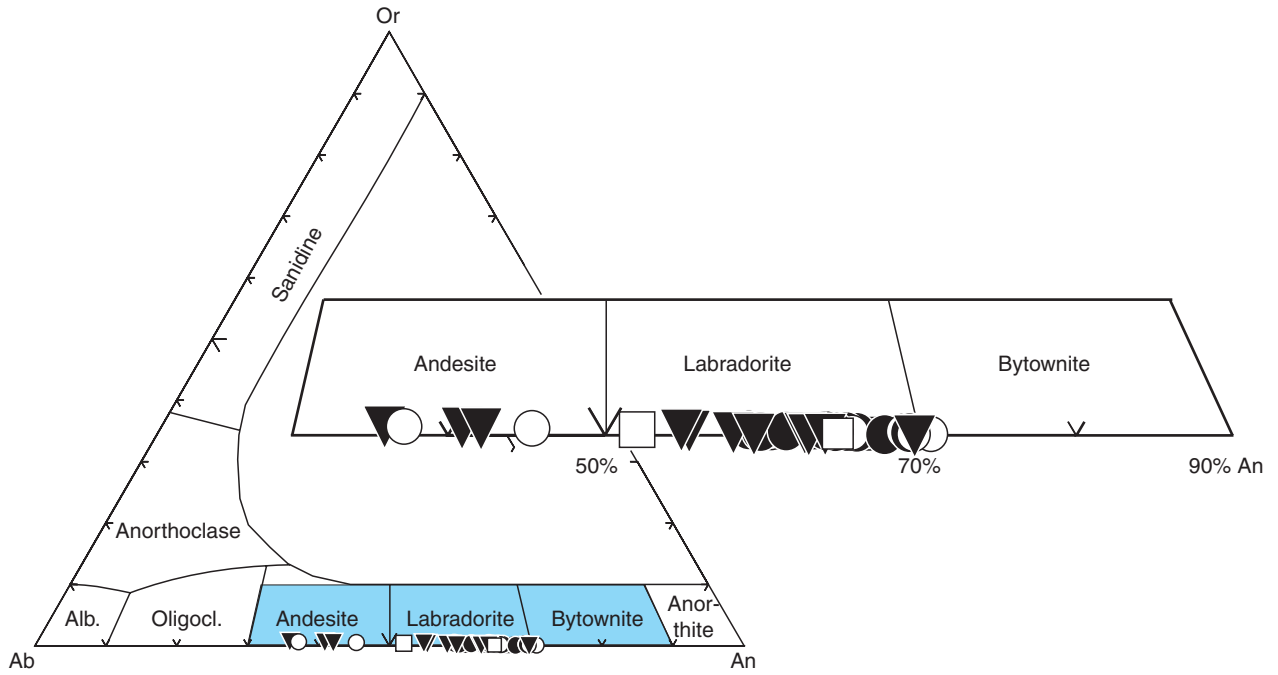


Figure F3. Clinopyroxene composition of Site 1224 ferrobasalts plotted in the conventional Wo-En-Fs classification scheme (Morimoto et al., 1988). Solid triangles = groundmass phases, open circles = phenocryst rims, solid circles = phenocryst cores.

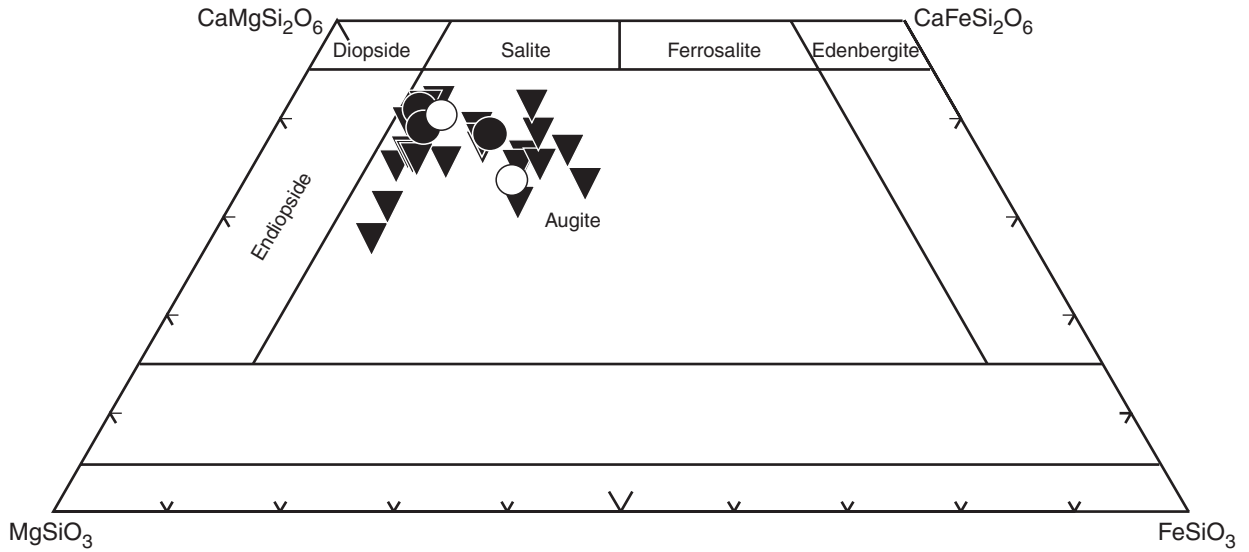


Figure F4. FeO-TiO₂-Fe₂O₃ diagram of opaque minerals from Site 1224 ferrobasalts. Solid triangles = groundmass phases, open circles = microphenocryst rims, solid circles = microphenocryst cores.

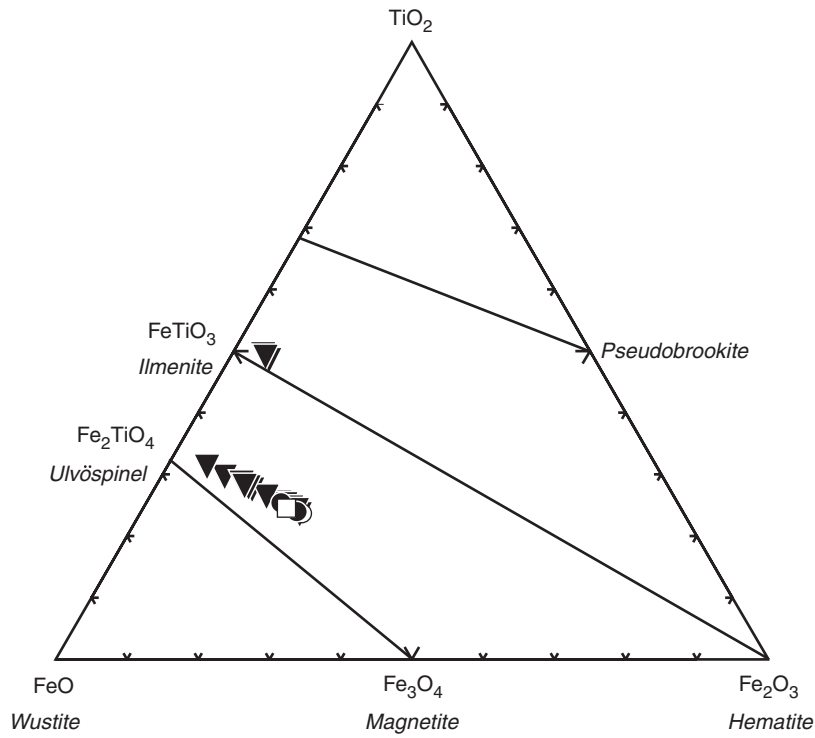


Figure F6. Quartz-alkali feldspar intergrowth found in Sample 200-1224F-3R-1, 14–16 cm, from lithostratigraphic Unit 1. Myr = myrmekite, Pl = plagioclase, Cpx = clinopyroxene, D-Gl = devitrified glass; Mt = Ti-magnetite.



Figure F7. A. FeO_{tot} vs. SiO_2 plot of myrmekite found in Site 1224 ferrobasalts. B. Cross, Iddings, Pirsson, and Washington (CIPW) normative quartz vs. CIPW $[100 \times \text{An}/(\text{An} + \text{Ab} + \text{Or})]$ plot of myrmekite found in Site 1224 ferrobasalts. C. CIPW normative orthoclase vs. CIPW plot of myrmekite found in Site 1224 ferrobasalts. Green circle = Hess Deep silicic melt composition, blue squares = experimental melts derived by low-pressure melting of oceanic cumulate gabbros (Koepke et al., 2004). D. Granitic portion of petrogeny's residua system for myrmekite found in Site 1224 ferrobasalts (solid circles). For comparison are experimental melts obtained by Dixon and Rutherford (1979), EPR dacite glass bleb (grey circle; Natland, 1991), DSDP Site 396 dacite globule from dolerite (white diamond; Sato, 1979), Hess Deep (green circle; Natland and Dick, 1996; Pedersen et al., 1996), ODP Site 735 plagiogranites, and low-pressure experimental melts of oceanic cumulate gabbros (blue field and white squares in the petrogeny's residua system inset; Koepke et al., 2004).

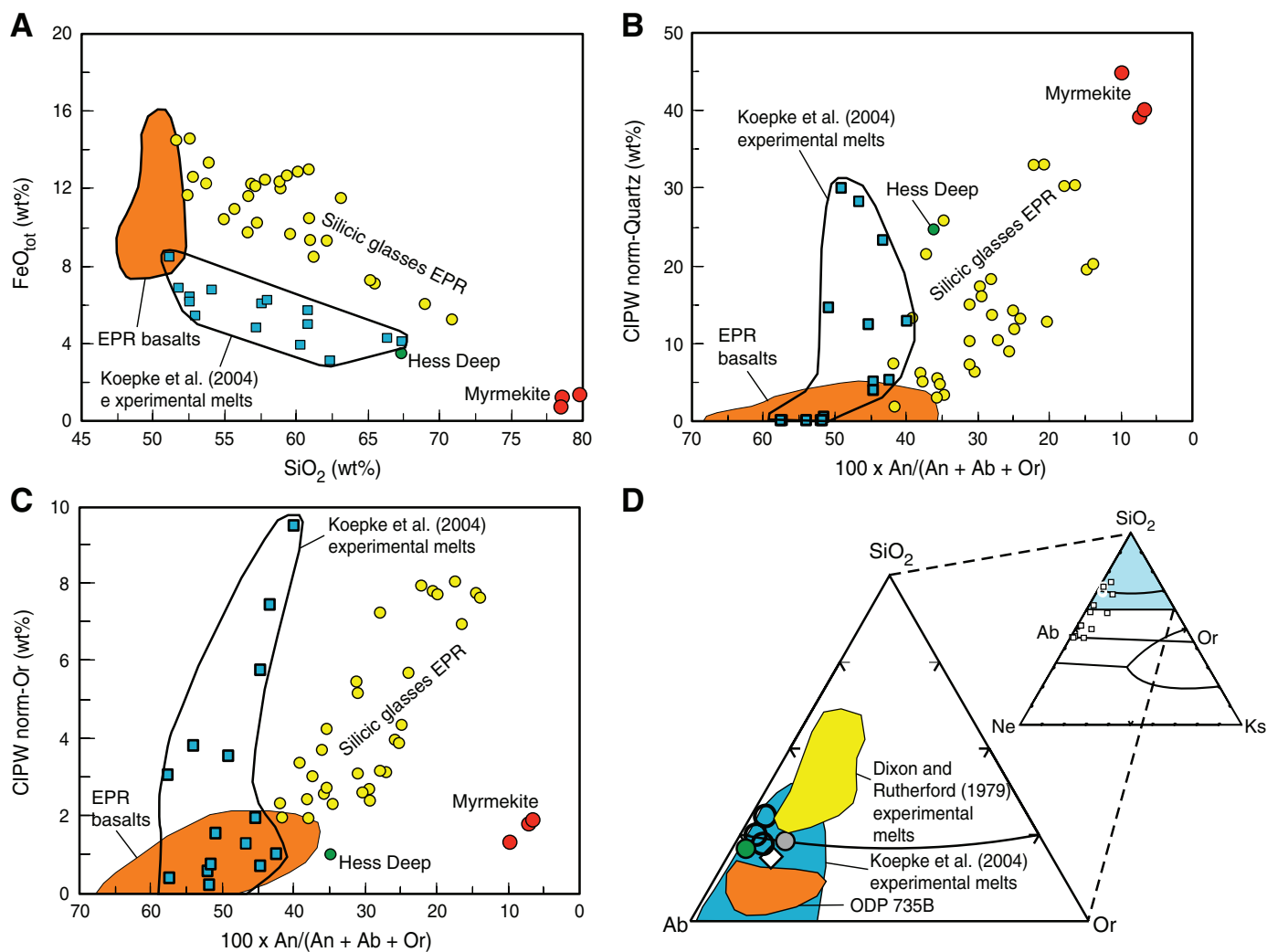


Figure F8. TiO_2 vs. MgO plot of Site 1224 EPM analyses of volcanic glasses (orange diamonds). Bulk composition of East Pacific Rise (EPR) andesites, EPR basalts (references in PETDB web database, www.petdb.org), Site 1224 ferrobasalts (Haraguchi and Ishi, this volume), experimental melts obtained at shallow pressures on oceanic cumulate gabbros (Koepke et al., 2004), and myrmekite (Myr) found in Site 1224 ferrobasalts are shown for comparison.

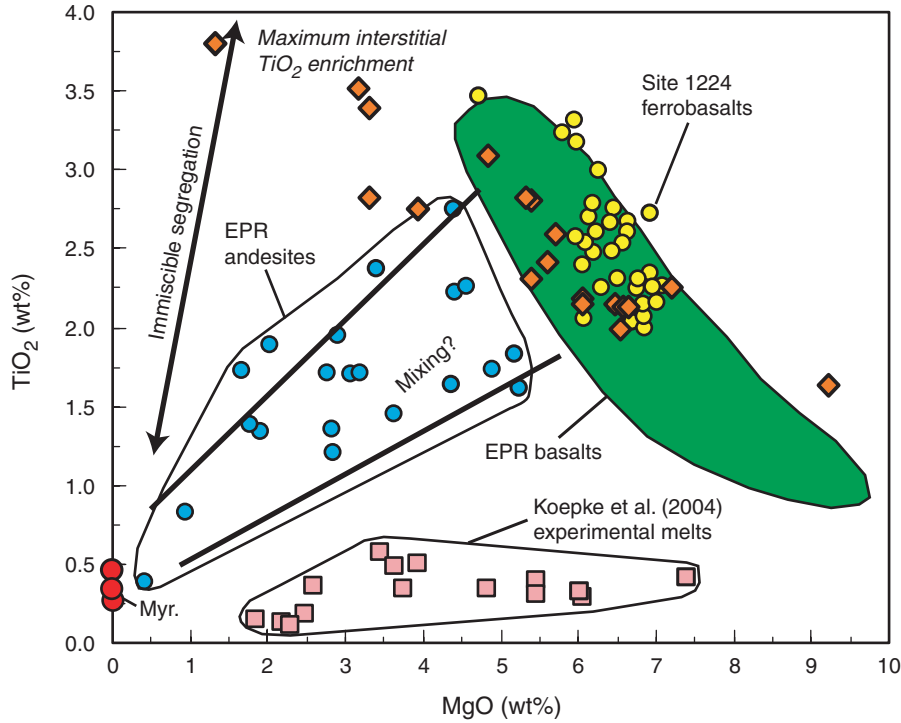


Table T1. Plagioclase compositions and structural formulas. (Continued on next page.)

Core, section, interval (cm)	Point	Phase	Major element oxide (wt%)										
			SiO ₂	TiO ₂	Al ₂ O ₃	Cr ₂ O ₃	FeO	MgO	CaO	K ₂ O	Na ₂ O	Total	
200-1224A-													
4X-1, 16-19	2-3	Plagioclase phenocryst rim	52.15	0.04	29.32	0.05	0.73	0.22	12.86	0.06	4.10	99.53	
	2-4	Plagioclase same phenocryst core	51.34	0.08	29.61	0.04	0.51	0.19	13.28	0.06	3.88	99.00	
	2-6	Plagioclase groundmass	52.34	0.04	29.28	0.01	0.83	0.19	12.64	0.07	4.14	99.54	
	1-1	Plagioclase microphenocryst	50.90	0.00	29.96	0.02	0.71	0.15	13.73	0.04	3.73	99.23	
200-1224D-													
3R-1, 50-53	1-1	Plagioclase groundmass	53.67	0.05	27.81	0.00	0.96	0.12	11.38	0.08	5.17	99.22	
	3-1	Plagioclase microphenocryst core	51.97	0.13	30.63	0.11	0.49	0.16	13.76	0.05	3.91	101.21	
	3-2	Plagioclase same microphenocryst rim	56.91	0.09	27.12	0.00	0.83	0.06	9.47	0.09	6.28	100.85	
	4-3	Plagioclase groundmass	54.39	0.16	28.25	0.00	0.93	0.12	11.43	0.08	5.15	100.51	
4R-1, 74-77	1-2	Plagioclase microphenocryst rim	50.22	0.03	30.78	0.00	0.63	0.22	14.20	0.04	3.43	99.55	
	1-3	Plagioclase microphenocryst core	50.19	0.13	30.14	0.01	0.62	0.18	13.79	0.03	3.36	98.46	
200-1224E-													
3R-1, 6-10	2-1	Plagioclase microphenocryst rim	51.58	0.08	30.02	0.07	0.82	0.15	13.40	0.04	3.85	100.02	
	2-2	Plagioclase same microphenocryst core	52.11	0.10	29.75	0.01	0.63	0.19	13.42	0.04	4.05	100.30	
200-1224F-													
1R-4, 115-117	1-6	Plagioclase groundmass	57.34	0.11	26.14		0.50	0.06	8.76	0.09	6.63	99.63	
	1-8	Plagioclase groundmass	52.41	0.04	28.89	0.00	0.70	0.17	12.25	0.05	4.61	99.13	
3R-1, 14-16	1-3	Plagioclase phenocryst rim	58.52	0.10	25.27	0.02	0.48	0.03	7.62	0.12	7.13	99.30	
	1-4	Plagioclase same phenocryst core	51.51	0.00	29.83	0.00	0.68	0.18	13.00	0.06	4.02	99.29	
	2-3	Plagioclase groundmass	59.16	0.00	25.23	0.01	0.36	0.02	7.33	0.11	7.24	99.47	
3R-3, 90-92	1-1	Big phenocryst plagioclase rim	52.08	0.02	28.98	0.03	0.87	0.19	12.49	0.04	4.48	99.18	
	1-2	Big phenocryst plagioclase mantle	49.76	0.06	30.47	0.02	0.59	0.20	13.96	0.04	3.46	98.57	
	1-3	Big phenocryst plagioclase core	49.75	0.10	30.52		0.58	0.21	14.29	0.01	3.31	98.77	
4R-6, 11-13	1-4	Plagioclase microphenocryst in pillow	51.21	0.08	29.99	0.01	0.65	0.22	13.39	0.01	3.81	99.37	
	2-1	Plagioclase phenocryst rim in pillow	49.72	0.04	30.94		0.78	0.22	14.42	0.02	3.30	99.44	
	2-2	Plagioclase phenocryst mantle in pillow	50.08	0.07	30.57	0.01	0.55	0.25	14.39	0.04	3.48	99.44	
	2-3	Plagioclase phenocryst core in pillow	50.35		30.61	0.01	0.79	0.23	14.14	0.03	3.43	99.60	
	3-3	Plagioclase	50.80	0.06	29.57	0.04	0.84	0.23	13.54	0.05	3.76	98.89	
6R-1, 29-34	1-1	Plagioclase in pillow	51.68	0.07	29.87	0.03	0.77	0.25	13.35	0.03	4.00	100.05	
	4-2	Plagioclase acicular in pillow	52.05		29.44	0.01	0.76	0.26	13.04	0.04	4.03	99.63	
6R-1, 105-107	1-3	Plagioclase phenocryst core	50.19	0.10	30.15		0.58	0.22	13.67	0.02	3.58	98.53	
	1-4	Plagioclase phenocryst rim	50.01	0.05	30.04	0.02	0.51	0.20	13.71	0.05	3.39	97.98	
11R-2, 13-15	1-1	Plagioclase groundmass	50.59	0.03	30.73	0.12	0.54	0.22	14.13	0.03	3.38	99.76	
	2-4	Plagioclase groundmass	51.88	0.02	29.52	0.00	0.84	0.20	12.97	0.04	4.20	99.67	
	5-1	Plagioclase microphenocryst	50.83	0.05	30.62	0.01	0.61	0.22	13.78	0.05	3.53	99.70	
13R-1, 22-24	1-1	Plagioclase microphenocryst core	53.12	0.03	28.58	0.13	0.69	0.18	11.76	0.07	4.48	99.05	
	1-5	Plagioclase groundmass	53.18	0.10	28.16	0.08	0.94	0.18	11.53	0.05	4.53	98.76	
15R-1, 88-90	1-1	Plagioclase microphenocryst	54.88		27.43	0.03	0.90	0.12	10.70	0.08	5.44	99.59	
	2-1	Big phenocryst plagioclase rim	52.19	0.08	28.89		0.89	0.16	12.54	0.05	4.38	99.18	
	2-2	Big phenocryst plagioclase mantle	52.41	0.07	29.49	0.02	0.68	0.18	12.53	0.05	4.32	99.76	
	2-3	Big phenocryst plagioclase core	52.52	0.01	29.28		0.72	0.16	12.33	0.05	4.53	99.61	
	3-3	Skeletal plagioclase groundmass	58.02	0.12	25.72	0.02	0.71	0.08	8.39	0.12	6.74	99.92	

Notes: In the Point column, the first number indicates the number of the circle drawn on the thin section, and the second number indicates the sequential number of analyses in that circle. Data in the Intergrowth column are the phases intergrown or associated with plagioclase. The first number indicates the table (e.g., 2 = clinopyroxene, 3 = glass, 4 = ophiolite, 5 = others), and the second number indicates the number of phases in that column. An = anorthite, Ab = albite, Or = orthoclase.

Table T1 (continued).

Core, section, interval (cm)	Point	Phase	Intergrowth	Trace element (ppm)									Total	An	Ab	Or
				Si	Ti	Al	Fe ³⁺	Ca	Na	K	Cr					
200-1224A-																
4X-1, 16-19	2-3	Plagioclase phenocryst rim	2-1, 2-2	9.5532	0.0061	6.3326	0.0747	2.5240	1.4574	0.0137	0.0073	19.9690	63.2	36.5	0.3	
	2-4	Plagioclase same phenocryst core	2-1, 2-2	9.4591	0.0115	6.4325	0.0525	2.6224	1.3873	0.0141	0.0053	19.9849	65.2	34.5	0.3	
	2-6	Plagioclase groundmass	2-1, 2-2	9.5805	0.0059	6.3173	0.0851	2.4783	1.4690	0.0166	0.0016	19.9544	62.5	37.1	0.4	
	1-1	Plagioclase microphenocryst		9.3747	0.0000	6.5047	0.0727	2.7097	1.3335	0.0083	0.0027	20.0062	66.9	32.9	0.2	
200-1224D-																
3R-1, 50-53	1-1	Plagioclase groundmass	2-3, 4-1	9.8338	0.0063	6.0075	0.0976	2.2350	1.8357	0.0184	0.0000	20.0344	54.7	44.9	0.4	
	3-1	Plagioclase microphenocryst core	2-5	9.3745	0.0181	6.5133	0.0490	2.6597	1.3667	0.0114	0.0152	20.0077	65.9	33.8	0.3	
	3-2	Plagioclase same microphenocryst rim	2-5	10.1790	0.0126	5.7186	0.0830	1.8152	2.1777	0.0209	0.0000	20.0070	45.2	54.3	0.5	
	4-3	Plagioclase groundmass	4-3, 4-4	9.8310	0.0213	6.0196	0.0935	2.2136	1.8058	0.0184	0.0000	20.0033	54.8	44.7	0.5	
4R-1, 74-77	1-2	Plagioclase microphenocryst rim	2-6	9.2356	0.0041	6.6728	0.0648	2.7979	1.2221	0.0086	0.0007	20.0066	69.5	30.3	0.2	
	1-3	Plagioclase microphenocryst core	2-6	9.3123	0.0183	6.5938	0.0637	2.7418	1.2104	0.0077	0.0011	19.9492	69.2	30.6	0.2	
200-1224E-																
3R-1, 6-10	2-1	Plagioclase microphenocryst rim	3-2, 3-3, 5-1	9.4178	0.0113	6.4623	0.0837	2.6213	1.3632	0.0083	0.0105	19.9784	65.7	34.1	0.2	
	2-2	Plagioclase same microphenocryst core	3-2, 3-3, 5-1	9.4826	0.0138	6.3819	0.0641	2.6171	1.4275	0.0103	0.0015	19.9988	64.5	35.2	0.3	
200-1224F-																
1R-4, 115-117	1-6	Plagioclase groundmass		10.3458	0.0149	5.5596	0.0501	1.6931	2.3208	0.0213	0.0000	20.0055	42.0	57.5	0.5	
	1-8	Plagioclase groundmass		9.6286	0.0061	6.2566	0.0719	2.4114	1.6412	0.0109	0.0004	20.0270	59.3	40.4	0.3	
3R-1, 14-16	1-3	Plagioclase phenocryst rim	2-10, 2-11, 5-4	10.5528	0.0132	5.3719	0.0486	1.4720	2.4941	0.0277	0.0029	19.9832	36.9	62.4	0.7	
	1-4	Plagioclase same phenocryst core	2-10, 2-11, 5-4	9.4622	0.0000	6.4593	0.0695	2.5588	1.4330	0.0144	0.0000	19.9971	63.9	35.8	0.4	
	2-3	Plagioclase groundmass	4-12, 5-5, 5-6	10.6229	0.0005	5.3419	0.0364	1.4106	2.5205	0.0245	0.0018	19.9591	35.7	63.7	0.6	
3R-3, 90-92	1-1	Big phenocryst plagioclase rim	2-12, 4-15	9.5802	0.0024	6.2854	0.0894	2.4623	1.5989	0.0102	0.0039	20.0326	60.5	39.3	0.3	
	1-2	Big phenocryst plagioclase mantle	2-12, 4-15	9.2383	0.0091	6.6697	0.0612	2.7767	1.2466	0.0101	0.0025	20.0142	68.8	30.9	0.3	
	1-3	Big phenocryst plagioclase core	2-12, 4-15	9.2211	0.0143	6.6694	0.0601	2.8387	1.1909	0.0012	0.0000	19.9958	70.4	29.5	0.0	
4R-6, 11-13	1-4	Plagioclase microphenocryst in pillow	3-5, 3-6, 2-13	9.4087	0.0114	6.4953	0.0661	2.6352	1.3589	0.0034	0.0008	19.9800	65.9	34.0	0.1	
	2-1	Plagioclase phenocryst rim in pillow	3-8	9.1687	0.0050	6.7272	0.0798	2.8498	1.1793	0.0056	0.0000	20.0153	70.6	29.2	0.1	
	2-2	Plagioclase phenocryst mantle in pillow	3-8	9.2310	0.0103	6.6422	0.0563	2.8421	1.2437	0.0085	0.0010	20.0351	69.4	30.4	0.2	
	2-3	Plagioclase phenocryst core in pillow	3-8	9.2593	0.0000	6.6368	0.0812	2.7865	1.2245	0.0075	0.0013	19.9970	69.3	30.5	0.2	
	3-3	Plagioclase	2-14, 2-15	9.4007	0.0086	6.4517	0.0866	2.6859	1.3494	0.0112	0.0052	19.9993	66.4	33.3	0.3	
6R-1, 29-34	1-1	Plagioclase in pillow	2-16, 3-9	9.4404	0.0099	6.4337	0.0781	2.6129	1.4164	0.0069	0.0047	20.0031	64.7	35.1	0.2	
	4-2	Plagioclase acicular in pillow	2-18, 2-19, 3-13	9.5325	0.0000	6.3573	0.0778	2.5588	1.4324	0.0105	0.0014	19.9707	63.9	35.8	0.3	
6R-1, 105-107	1-3	Plagioclase phenocryst core	2-20, 4-17, 4-18	9.3116	0.0144	6.5951	0.0601	2.7179	1.2892	0.0054	0.0000	19.9937	67.7	32.1	0.1	
	1-4	Plagioclase phenocryst rim	2-20, 4-17, 4-18	9.3222	0.0071	6.6021	0.0528	2.7374	1.2243	0.0112	0.0025	19.9597	68.9	30.8	0.3	
11R-2, 13-15	1-1	Plagioclase groundmass	3-15, 2-22	9.2717	0.0042	6.6412	0.0549	2.7741	1.2009	0.0081	0.0169	19.9721	69.6	30.2	0.2	
	2-4	Plagioclase groundmass	3-16, 3-17, 2-23	9.5028	0.0031	6.3750	0.0854	2.5464	1.4930	0.0097	0.0000	20.0153	62.9	36.9	0.2	
	5-1	Plagioclase microphenocryst		9.3143	0.0072	6.6150	0.0624	2.7059	1.2555	0.0110	0.0011	19.9725	68.1	31.6	0.3	
13R-1, 22-24	1-1	Plagioclase microphenocryst core	2-25	9.7381	0.0038	6.1774	0.0706	2.3108	1.5923	0.0163	0.0195	19.9287	59.0	40.6	0.4	
	1-5	Plagioclase groundmass	2-26, 4-20	9.7820	0.0142	6.1059	0.0969	2.2716	1.6161	0.0122	0.0118	19.9107	58.2	41.4	0.3	
15R-1, 88-90	1-1	Plagioclase microphenocryst	4-21	9.9861	0.0000	5.8846	0.0917	2.0865	1.9209	0.0178	0.0050	19.9926	51.8	47.7	0.4	
	2-1	Big phenocryst plagioclase rim		9.5956	0.0108	6.2622	0.0910	2.4709	1.5613	0.0117	0.0000	20.0035	61.1	38.6	0.3	
	2-2	Big phenocryst plagioclase mantle		9.5670	0.0097	6.3449	0.0694	2.4501	1.5274	0.0123	0.0035	19.9843	61.4	38.3	0.3	
	2-3	Big phenocryst plagioclase core		9.5996	0.0020	6.3086	0.0735	2.4148	1.6069	0.0107	0.0000	20.0161	59.9	39.9	0.3	
	3-3	Skeletal plagioclase groundmass	2-29, 2-30	10.4350	0.0167	5.4534	0.0711	1.6174	2.3513	0.0274	0.0022	19.9744	40.5	58.8	0.7	

Table T2. Clinopyroxene compositions with structural formulas. (Continued on next two pages.)

Core, section, interval (cm)	Point	Phase	Name	Major element oxide (wt%)										
				SiO ₂	TiO ₂	Al ₂ O ₃	Cr ₂ O ₃	FeO	MnO	MgO	CaO	Na ₂ O	Total	
200-1224A-														
4X-1, 16-19	2-1	Clinopyroxene phenocryst rim	Aluminian augite	51.84	0.71	2.45	0.32	7.73	0.06	16.18	19.47	0.28	99.05	
	2-2	Clinopyroxene same phenocryst core	Augite	51.58	0.69	2.23	0.19	7.37	0.06	16.09	19.45	0.31	97.97	
200-1224D-														
3R-1, 50-53	1-2	Clinopyroxene groundmass	Augite	51.14	1.08	2.16	0.09	10.70	0.34	15.00	18.87	0.27	99.65	
	2-1	Clinopyroxene groundmass	Augite	51.50	1.16	2.08	0.07	11.28	0.34	15.09	18.41	0.30	100.21	
	3-3	Clinopyroxene groundmass	Augite	50.03	0.87	1.25	0.02	17.57	0.55	12.29	15.61	0.25	98.46	
4R-1, 74-77	1-1	Clinopyroxene groundmass	Aluminian augite	50.43	1.15	3.10	0.09	9.99	0.25	16.25	16.87	0.30	98.43	
200-1224F-														
1R-4, 115-117	1-2	Clinopyroxene groundmass	Aluminian augite	49.68	1.39	2.41		13.90	0.36	14.10	16.68	0.33	98.85	
	1-3	Clinopyroxene phenocryst rim	Aluminian augite	51.38	0.79	2.39	0.19	8.25	0.13	16.12	19.54	0.29	99.06	
	1-4	Clinopyroxene phenocryst core	Augite	52.00	0.74	2.26	0.19	7.91	0.29	16.66	19.02	0.26	99.33	
200-1224D-														
3R-1, 14-16	1-5	Clinopyroxene groundmass	Augite	50.60	0.90	1.71	0.05	13.87	0.42	13.78	17.13	0.30	98.76	
	1-6	Clinopyroxene groundmass	Aluminian augite	50.73	1.13	2.41	0.11	11.55	0.34	15.03	17.74	0.30	99.33	
200-1224F-														
3R-3, 90-92	1-4	Clinopyroxene groundmass	Aluminian augite	48.53	1.75	2.86		14.77	0.38	13.24	16.49	0.42	98.45	
4R-6, 11-13	1-1	Clinopyroxene groundmass in pillow	Aluminian chromian augite	51.44	0.72	3.21	0.58	6.93	0.20	16.91	19.01	0.26	99.26	
	3-1	Clinopyroxene glomrule	Aluminian augite	51.35	0.99	3.23	0.12	7.79	0.17	17.39	17.53	0.26	98.84	
	3-2	Clinopyroxene glomrule	Aluminian augite	50.27	1.18	4.18	0.28	8.07	0.17	17.09	17.04	0.26	98.55	
6R-1, 29-34	1-5	Clinopyroxene in pillow	Augite	53.70	0.32	1.48	0.34	8.68	0.38	20.85	13.87	0.19	99.81	
	2-3	Clinopyroxene in pillow	Augite	52.95	0.49	1.60	0.27	7.84	0.21	18.60	17.39	0.17	99.51	
	4-1	Clinopyroxene in black glass pillow	Aluminian augite	51.50	1.03	3.40	0.16	7.56	0.22	16.83	18.76	0.29	99.76	
	4-4	Clinopyroxene in pillow	Augite	52.93	0.63	1.82	0.24	8.45	0.27	19.37	15.16	0.22	99.09	
6R-1, 105-107	1-2	Clinopyroxene groundmass	Aluminian chromian augite	50.41	0.82	3.59	0.34	7.20	0.19	15.80	19.42	0.31	98.09	
	1-5	Clinopyroxene groundmass	Aluminian augite	50.32	0.94	3.49	0.28	8.35	0.27	17.13	17.07	0.26	98.12	
11R-2, 13-15	1-2	Clinopyroxene groundmass	Aluminian augite	50.70	1.03	3.96	0.27	7.75	0.15	15.82	18.80	0.30	98.76	
	2-1	Clinopyroxene groundmass	Aluminian augite	50.54	0.87	3.94	0.21	7.76	0.24	15.42	18.74	0.31	98.03	
	4-1	Clinopyroxene groundmass	Aluminian augite	51.18	0.98	3.47	0.22	7.80	0.25	15.53	19.91	0.26	99.60	
13R-1, 22-24	1-2	Clinopyroxene groundmass	Aluminian augite	49.21	1.50	2.34	0.06	15.56	0.60	12.18	17.14	0.30	98.90	
	1-6	Clinopyroxene groundmass	Augite	50.99	1.16	1.74	0.02	15.02	0.40	14.88	14.99	0.25	99.45	
15R-1, 88-90	1-3	Clinopyroxene microphenocryst core	Aluminian augite	50.65	1.13	2.36	0.05	11.03	0.26	14.41	18.36	0.32	98.57	
	1-4	Same clinopyroxene microphenocryst rim	Aluminian augite	49.61	1.43	2.97		13.64	0.44	14.54	15.94	0.30	98.86	
	3-1	Clinopyroxene groundmass	Aluminian augite	48.81	1.83	2.91	0.04	13.66	0.32	12.68	17.83	0.34	98.42	
	3-4	Clinopyroxene groundmass	Aluminian augite	48.93	1.86	3.36	0.03	12.74	0.26	12.53	19.39	0.40	99.50	

Note: In the Point column, the first number indicates the number of the circle drawn on the thin section, and the second number indicates the sequential number of analyses in that circle. En = enstatite, Fs = ferrosilite, Wo = wollastonite.

Table T2 (continued).

Core, section, interval (cm)	Point	Phase	Name	Trace element (ppm)													
				Si	Ti	Al (T)	Al (M1)	Fe ³⁺ _(T)	Fe ³⁺ _(M1)	Fe ²⁺	Mn	Mg	Ca	Na	Cr	Total	
200-1224A-																	
4X-1, 16-19	2-1	Clinopyroxene phenocryst rim	Aluminian augite	1.9279	0.0199	0.0721	0.0355	0.0000	0.0079	0.2324	0.0018	0.8968	0.7757	0.0205	0.0094	4.0000	
	2-2	Clinopyroxene same phenocryst core	Augite	1.9370	0.0194	0.0630	0.0358	0.0000	0.0052	0.2262	0.0019	0.9007	0.7824	0.0226	0.0057	4.0000	
200-1224D-																	
3R-1, 50-53	1-2	Clinopyroxene groundmass	Augite	1.9132	0.0304	0.0868	0.0085	0.0000	0.0346	0.3002	0.0109	0.8365	0.7564	0.0198	0.0028	4.0000	
	2-1	Clinopyroxene groundmass	Augite	1.9185	0.0324	0.0815	0.0096	0.0000	0.0264	0.3249	0.0107	0.8380	0.7346	0.0214	0.0020	4.0000	
	3-3	Clinopyroxene groundmass	Augite	1.9452	0.0256	0.0548	0.0027	0.0000	0.0192	0.5521	0.0183	0.7125	0.6501	0.0189	0.0007	4.0000	
4R-1, 74-77	1-1	Clinopyroxene groundmass	Aluminian augite	1.8948	0.0325	0.1052	0.0321	0.0000	0.0272	0.2868	0.0079	0.9101	0.6791	0.0217	0.0027	4.0000	
200-1224F-																	
1R-4, 115-117	1-2	Clinopyroxene groundmass	Aluminian augite	1.8922	0.0398	0.1078	0.0003	0.0000	0.0523	0.3906	0.0116	0.8005	0.6806	0.0244	0.0000	4.0000	
	1-3	Clinopyroxene phenocryst rim	Aluminian augite	1.9125	0.0220	0.0875	0.0172	0.0000	0.0416	0.2151	0.0041	0.8944	0.7791	0.0209	0.0056	4.0000	
	1-4	Clinopyroxene phenocryst core	Augite	1.9267	0.0205	0.0733	0.0255	0.0000	0.0199	0.2252	0.0091	0.9202	0.7552	0.0187	0.0057	4.0000	
200-1224D-																	
3R-1, 14-16	1-5	Clinopyroxene groundmass	Augite	1.9318	0.0259	0.0682	0.0087	0.0000	0.0286	0.4144	0.0136	0.7840	0.7006	0.0225	0.0016	4.0000	
	1-6	Clinopyroxene groundmass	Aluminian augite	1.9065	0.0321	0.0935	0.0130	0.0000	0.0347	0.3283	0.0107	0.8421	0.7143	0.0216	0.0033	4.0000	
200-1224F-																	
3R-3, 90-92	1-4	Clinopyroxene groundmass	Aluminian augite	1.8643	0.0506	0.1296	0.0000	0.0061	0.0660	0.4024	0.0123	0.7584	0.6786	0.0316	0.0000	4.0000	
4R-6, 11-13	1-1	Clinopyroxene groundmass in pillow	Aluminian chromian augite	1.9004	0.0200	0.0996	0.0400	0.0000	0.0212	0.1929	0.0063	0.9315	0.7525	0.0186	0.0169	4.0000	
	3-1	Clinopyroxene glomrule	Aluminian augite	1.9040	0.0276	0.0960	0.0453	0.0000	0.0102	0.2315	0.0054	0.9615	0.6965	0.0184	0.0037	4.0000	
	3-2	Clinopyroxene glomrule	Aluminian augite	1.8717	0.0331	0.1283	0.0552	0.0000	0.0173	0.2341	0.0054	0.9484	0.6797	0.0186	0.0082	4.0000	
6R-1, 29-34	1-5	Clinopyroxene in pillow	Augite	1.9557	0.0088	0.0443	0.0191	0.0000	0.0108	0.2535	0.0117	1.1321	0.5411	0.0131	0.0098	4.0000	
	2-3	Clinopyroxene in pillow	Augite	1.9460	0.0135	0.0540	0.0152	0.0000	0.0161	0.2248	0.0066	1.0190	0.6849	0.0121	0.0078	4.0000	
	4-1	Clinopyroxene in black glass pillow	Aluminian augite	1.8956	0.0286	0.1044	0.0430	0.0000	0.0203	0.2124	0.0068	0.9234	0.7398	0.0209	0.0048	4.0000	
	4-4	Clinopyroxene in pillow	Augite	1.9501	0.0176	0.0499	0.0293	0.0000	0.0000	0.2602	0.0083	1.0635	0.5986	0.0155	0.0071	4.0000	
6R-1, 105-107	1-2	Clinopyroxene groundmass	Aluminian chromian augite	1.8901	0.0232	0.1099	0.0487	0.0000	0.0274	0.1984	0.0062	0.8832	0.7802	0.0227	0.0100	4.0000	
	1-5	Clinopyroxene groundmass	Aluminian augite	1.8827	0.0265	0.1173	0.0367	0.0000	0.0380	0.2234	0.0086	0.9555	0.6844	0.0187	0.0082	4.0000	
11R-2, 13-15	1-2	Clinopyroxene groundmass	Aluminian augite	1.8910	0.0288	0.1090	0.0650	0.0000	0.0000	0.2416	0.0046	0.8798	0.7510	0.0213	0.0078	4.0000	
	2-1	Clinopyroxene groundmass	Aluminian augite	1.9007	0.0246	0.0993	0.0755	0.0000	0.0000	0.2442	0.0077	0.8644	0.7550	0.0224	0.0062	4.0000	
	4-1	Clinopyroxene groundmass	Aluminian augite	1.8974	0.0272	0.1026	0.0489	0.0000	0.0119	0.2300	0.0078	0.8581	0.7909	0.0189	0.0063	4.0000	
13R-1, 22-24	1-2	Clinopyroxene groundmass	Aluminian augite	1.8968	0.0435	0.1032	0.0031	0.0000	0.0338	0.4676	0.0196	0.6999	0.7080	0.0226	0.0019	4.0000	
	1-6	Clinopyroxene groundmass	Augite	1.9323	0.0332	0.0677	0.0100	0.0000	0.0090	0.4671	0.0128	0.8405	0.6086	0.0182	0.0006	4.0000	
15R-1, 88-90	1-3	Clinopyroxene microphenocryst core	Aluminian augite	1.9198	0.0321	0.0802	0.0252	0.0000	0.0127	0.3370	0.0083	0.8142	0.7456	0.0234	0.0015	4.0000	
	1-4	Same clinopyroxene microphenocryst rim	Aluminian augite	1.8846	0.0408	0.1154	0.0174	0.0000	0.0386	0.3946	0.0143	0.8232	0.6489	0.0221	0.0000	4.0000	
	3-1	Clinopyroxene groundmass	Aluminian augite	1.8770	0.0530	0.1230	0.0090	0.0000	0.0324	0.4070	0.0103	0.7267	0.7348	0.0256	0.0012	4.0000	
	3-4	Clinopyroxene groundmass	Aluminian augite	1.8564	0.0529	0.1436	0.0067	0.0000	0.0598	0.3446	0.0084	0.7089	0.7882	0.0296	0.0009	4.0000	

Table T2 (continued).

Core, section, interval (cm)	Point	Phase	Name	En	Fs	Wo	Mg#	Cr#
200-1224A-								
4X-1, 16-19	2-1	Clinopyroxene phenocryst rim	Aluminian augite	46.8	12.6	40.5	0.79	0.08
	2-2	Clinopyroxene same phenocryst core	Augite	47.0	12.2	40.8	0.80	0.05
200-1224D-								
3R-1, 50-53	1-2	Clinopyroxene groundmass	Augite	43.15	17.83	39.02	0.74	0.03
	2-1	Clinopyroxene groundmass	Augite	43.3	18.7	38.0	0.72	0.02
	3-3	Clinopyroxene groundmass	Augite	36.5	30.2	33.3	0.56	0.01
4R-1, 74-77	1-1	Clinopyroxene groundmass	Aluminian augite	47.6	16.8	35.5	0.76	0.02
200-1224F-								
1R-4, 115-117	1-2	Clinopyroxene groundmass	Aluminian augite	41.4	23.5	35.2	0.67	0.00
	1-3	Clinopyroxene phenocryst rim	Aluminian augite	46.2	13.5	40.3	0.81	0.05
	1-4	Clinopyroxene phenocryst core	Augite	47.7	13.2	39.1	0.80	0.05
200-1224D-								
3R-1, 14-16	1-5	Clinopyroxene groundmass	Augite	40.4	23.5	36.1	0.65	0.02
	1-6	Clinopyroxene groundmass	Aluminian augite	43.6	19.4	37.0	0.72	0.03
200-1224F-								
3R-3, 90-92	1-4	Clinopyroxene groundmass	Aluminian augite	39.4	25.3	35.3	0.65	0.00
4R-6, 11-13	1-1	Clinopyroxene groundmass in pillow	Aluminian chromian augite	48.9	11.6	39.5	0.83	0.11
	3-1	Clinopyroxene glomrule	Aluminian augite	50.5	13.0	36.6	0.81	0.03
	3-2	Clinopyroxene glomrule	Aluminian augite	50.3	13.6	36.1	0.80	0.04
6R-1, 29-34	1-5	Clinopyroxene in pillow	Augite	58.1	14.2	27.8	0.82	0.13
	2-3	Clinopyroxene in pillow	Augite	52.22	12.68	35.10	0.82	0.10
	4-1	Clinopyroxene in black glass pillow	Aluminian augite	48.53	12.59	38.88	0.81	0.03
	4-4	Clinopyroxene in pillow	Augite	55.09	13.91	31.00	0.80	0.08
6R-1, 105-107	1-2	Clinopyroxene groundmass	Aluminian chromian augite	46.60	12.24	41.17	0.82	0.06
	1-5	Clinopyroxene groundmass	Aluminian augite	50.03	14.14	35.83	0.81	0.05
11R-2, 13-15	1-2	Clinopyroxene groundmass	Aluminian augite	46.87	13.12	40.01	0.78	0.04
	2-1	Clinopyroxene groundmass	Aluminian augite	46.19	13.46	40.35	0.78	0.03
	4-1	Clinopyroxene groundmass	Aluminian augite	45.19	13.15	41.66	0.79	0.04
13R-1, 22-24	1-2	Clinopyroxene groundmass	Aluminian augite	36.28	27.01	36.71	0.60	0.02
	1-6	Clinopyroxene groundmass	Augite	43.37	25.23	31.40	0.64	0.01
15R-1, 88-90	1-3	Clinopyroxene microphenocryst core	Aluminian augite	42.45	18.67	38.87	0.71	0.01
	1-4	Same clinopyroxene microphenocryst rim	Aluminian augite	42.89	23.31	33.80	0.68	0.00
	3-1	Clinopyroxene groundmass	Aluminian augite	38.02	23.53	38.45	0.64	0.01
	3-4	Clinopyroxene groundmass	Aluminian augite	37.12	21.61	41.27	0.67	0.01

Table T3. Composition of olivine microphenocryst.

Core, section, interval (cm)	Point	Phase	Major element oxide (wt%)												
			SiO ₂	TiO ₂	Al ₂ O ₃	Cr ₂ O ₃	FeO	MnO	MgO	CaO	K ₂ O	Na ₂ O	BaO	P ₂ O ₅	Total
200-1224F- 11R-2, 13-15	3-1	Olivine microphenocryst	38.68	0.10	0.00	0.05	19.88	0.31	39.80	0.35	0.01	0.00	0.07	0.05	99.31

Note: In the Point column, the first number indicates the number of the circle drawn on the thin section, and the second number indicates the sequential number of analyses in that circle.

Table T4. Composition of opaque minerals. (Continued on next page.)

Core, section, interval (cm)	Point	Phase	Major element oxide (wt%)								
			SiO ₂	TiO ₂	Al ₂ O ₃	Cr ₂ O ₃	FeO	MnO	MgO	Total	
200-1224D-											
3R-1, 50–53	1-3	Octahedral solid solution groundmass	0.41	22.96	1.67	0.15	70.57	0.50	1.02	97.29	
	2-2	Octahedral solid solution skeletal	0.28	24.57	1.65	0.00	71.19	0.46	0.99	99.14	
	4-1	Octahedral solid solution microphenocryst core	0.35	24.77	1.49		69.99	0.56	0.84	98.00	
	4-2	Octahedral solid solution same microphenocryst rim	0.60	23.31	1.89		69.98	0.79	0.63	97.19	
4R-1, 74–77	1-4	Octahedral solid solution groundmass	0.39	25.11	1.84	0.02	67.20	0.69	0.15	95.39	
200-1224F-											
1R-4, 115–117	1-1	Octahedral solid solution groundmass	0.38	23.61	0.97	0.08	70.69	0.73	0.31	96.77	
	1-5	Octahedral solid solution groundmass	0.42	27.80	1.15	0.07	65.30	0.58	0.44	95.76	
	1-7	Octahedral solid solution groundmass skeletal	0.57	24.32	1.48		69.05	0.65	0.37	96.44	
200-1224D-											
3R-1, 14–16	1-1	Octahedral solid solution microphenocryst core	0.30	23.00	1.43	0.09	71.50	0.51	0.66	97.49	
	1-2	Octahedral solid solution same microphenocryst rim	0.42	22.42	1.11	0.06	71.07	0.68	0.62	96.39	
	2-4	Rhombohedral solid solution groundmass	0.36	50.31			46.98	0.65	0.97	99.27	
	2-5	Rhombohedral solid solution groundmass	0.90	48.13	0.13	0.00	46.88	0.58	0.57	97.19	
	2-6	Rhombohedral solid solution groundmass	0.30	49.98	0.01	0.06	47.57	0.59	0.77	99.28	
200-1224F-											
3R-3, 90–92	1-5	Octahedral solid solution groundmass	1.07	28.35	1.15	0.05	57.50	0.57	0.19	88.88	
	1-9	Octahedral solid solution groundmass	1.39	28.82	1.60	0.07	58.52	0.71	0.22	91.33	
6R-1, 105–107	1-1	Octahedral solid solution groundmass	0.69	25.27	1.77	0.06	61.93	0.37	0.55	90.65	
	1-6	Octahedral solid solution groundmass	1.37	25.26	2.11	0.03	61.09	0.62	0.70	91.18	
13R-1, 22–24	1-3	Octahedral solid solution groundmass	0.48	24.97	2.00	0.11	62.46	0.57	0.70	91.30	
	1-4	Octahedral solid solution groundmass	1.09	26.89	2.26	0.10	59.59	0.52	0.72	91.18	
15R-1, 88–90	1-2	Octahedral solid solution microphenocryst	0.41	23.55	2.11	0.02	70.20	0.53	0.85	97.66	
	3-2	Octahedral solid solution groundmass	0.31	22.28	2.05	0.06	71.17	0.57	0.18	96.62	

Notes: In the Point column, the first number indicates the number of the circle drawn on the thin section, and the second number indicates the sequential number of analyses in that circle.
Ilm = ilmenite, Usp = ulvöspinel.

Table T4 (continued).

Core, section, interval (cm)	Point	Phase	Trace element (ppm)							Total	Ilm	Usp	Mg#
			Ti	Al	Fe ³⁺	Fe ²⁺	Mn	Mg	Cr				
200-1224D-													
3R-1, 50-53	1-3	Octahedral solid solution groundmass	0.7002	0.0800	0.6320	1.5724	0.0172	0.0615	0.0049	3.0682		0.69	0.04
	2-2	Octahedral solid solution skeletal	0.7297	0.0768	0.5740	1.6088	0.0153	0.0585	0.0000	3.0632		0.72	0.03
	4-1	Octahedral solid solution microphenocryst core	0.7440	0.0703	0.5486	1.6287	0.0188	0.0502	0.0000	3.0606		0.73	0.03
	4-2	Octahedral solid solution same microphenocryst rim	0.7117	0.0903	0.5999	1.5981	0.0272	0.0379	0.0000	3.0650		0.70	0.02
4R-1, 74-77	1-4	Octahedral solid solution groundmass	0.7703	0.0885	0.4650	1.6946	0.0238	0.0091	0.0006	3.0519		0.77	0.01
200-1224F-													
1R-4, 115-117	1-1	Octahedral solid solution groundmass	0.7283	0.0469	0.6084	1.6321	0.0254	0.0187	0.0027	3.0625		0.71	0.01
	1-5	Octahedral solid solution groundmass	0.8389	0.0543	0.3392	1.7593	0.0196	0.0264	0.0023	3.0399		0.83	0.01
	1-7	Octahedral solid solution groundmass skeletal	0.7462	0.0712	0.5423	1.6537	0.0225	0.0225	0.0000	3.0585		0.73	0.01
200-1224D-													
3R-1, 14-16	1-1	Octahedral solid solution microphenocryst core	0.7027	0.0685	0.6416	1.5932	0.0177	0.0401	0.0028	3.0667		0.69	0.02
	1-2	Octahedral solid solution same microphenocryst rim	0.6975	0.0539	0.6708	1.5820	0.0239	0.0384	0.0019	3.0684		0.68	0.02
	2-4	Rhombohedral solid solution groundmass	0.9705	0.0000	0.0873	0.9058	0.0140	0.0372	0.0000	2.0149	0.96		0.04
	2-5	Rhombohedral solid solution groundmass	0.9595	0.0041	0.1131	0.9067	0.0130	0.0224	0.0000	2.0188	0.94		0.02
	2-6	Rhombohedral solid solution groundmass	0.9663	0.0003	0.0972	0.9090	0.0128	0.0295	0.0012	2.0164	0.95		0.03
200-1224F-													
3R-3, 90-92	1-5	Octahedral solid solution groundmass	0.9113	0.0579	0.1541	1.8615	0.0207	0.0122	0.0016	3.0193		0.92	0.01
	1-9	Octahedral solid solution groundmass	0.9020	0.0785	0.1508	1.8473	0.0249	0.0135	0.0023	3.0192		0.92	0.01
6R-1, 105-107	1-1	Octahedral solid solution groundmass	0.8075	0.0889	0.3739	1.7239	0.0133	0.0348	0.0020	3.0442		0.81	0.02
	1-6	Octahedral solid solution groundmass	0.8049	0.1053	0.3614	1.7055	0.0221	0.0440	0.0011	3.0441		0.82	0.02
13R-1, 22-24	1-3	Octahedral solid solution groundmass	0.7908	0.0993	0.3994	1.6902	0.0203	0.0441	0.0038	3.0478		0.80	0.03
	1-4	Octahedral solid solution groundmass	0.8433	0.1113	0.2565	1.7553	0.0185	0.0445	0.0034	3.0327		0.87	0.02
15R-1, 88-90	1-2	Octahedral solid solution microphenocryst	0.7112	0.0997	0.5893	1.5951	0.0181	0.0507	0.0008	3.0649		0.71	0.03
	3-2	Octahedral solid solution groundmass	0.6875	0.0989	0.6426	1.6037	0.0198	0.0112	0.0020	3.0658		0.68	0.01

Table T5. Composition of volcanic glass and palagonite.

Core, section, interval (cm)	Point	Phase	Type	Major element oxide (wt%)												
				SiO ₂	TiO ₂	Al ₂ O ₃	Cr ₂ O ₃	FeO	MnO	MgO	CaO	Na ₂ O	K ₂ O	P ₂ O ₅	Cl	Total
200-1224A- 4X-1, 16-19	1-1	Black glass	S	50.76	1.64	13.17	0.00	10.36	0.17	9.25	10.84	2.46	0.06	0.13	0.00	98.83
200-1224E- 3R-1, 6-10	2-3	Brown glass	G	49.55	2.81	12.55	0.10	14.16	0.30	5.39	9.79	2.90	0.17	0.22	0.07	98.00
	2-4	Palagonite	P	46.77	3.53	9.43	0.01	23.75	0.02	3.18	1.03	0.62	3.91	0.00	0.15	92.40
	1-1	Brown glass	G	49.43	2.82	12.87	0.07	14.17	0.30	5.32	9.86	2.88	0.18	0.18	0.09	98.16
200-1224F- 4R-6, 11-13	1-2	Fresh glass in pillow	G	49.75	2.16	13.58		12.22	0.18	6.49	10.89	2.75	0.13	0.20	0.06	98.41
	1-3	Fresh glass in pillow	S	51.04	2.19	13.83		13.11	0.30	6.05	10.51	0.29	0.15	0.18	0.03	97.67
	1-5	Fresh glass in pillow	G	49.79	2.13	13.59	0.01	12.12	0.28	6.60	10.80	2.79	0.15	0.22	0.06	98.53
	2-5	Black glass in pillow	S	48.69	2.31	14.04	0.01	13.79	0.19	5.41	10.90	2.95	0.20	0.16	0.04	98.71
6R-1, 29-34	1-2	Brown glass pillow	G	49.60	2.00	13.46	0.03	12.25	0.30	6.54	10.73	2.67	0.13	0.13	0.01	97.86
	1-3	Orange glass pillow	P	46.95	2.82	13.11	0.01	18.98	0.03	3.31	0.52	2.14	3.55	0.05	0.26	91.73
	1-4	Reddish glass pillow	P	47.94	2.76	10.67	0.02	21.12	0.01	3.92	0.63	0.86	3.65	0.07	0.20	91.86
	2-1	Clear glass pillow	P	49.58	3.10	9.27	0.04	19.72		4.84	0.67	0.28	4.28	0.01	0.02	91.80
	4-3	Glass near pl in pillow	S	50.36	2.14	13.75	0.01	12.99	0.24	6.07	10.50	1.49	0.11	0.16	0.01	97.83
	4-5	Glass in pillow	S	49.94	2.13	13.60	0.02	11.97	0.34	6.65	10.82	2.81	0.14	0.18	0.05	98.67
11R-2, 13-15	1-3	Glass	S	49.45	2.25	12.41	0.08	13.70	0.35	7.22	11.09	2.52	0.13	0.21	0.05	99.45
	2-2	Brown glass	G	49.66	2.59	13.00	0.06	13.40	0.20	5.71	10.07	2.86	0.19	0.23	0.08	98.04
	2-3	Palagonite	P	40.35	3.80	8.75	0.03	20.25	0.02	1.33	1.01	6.55	2.41	0.04	0.06	84.61
	3-2	Yellow glass	P	46.56	3.39	8.69	0.02	21.92	0.00	3.30	0.92	1.70	3.71	0.04	0.15	90.41
	4-2	Brown glass	G	49.96	2.42	13.14	0.06	13.22	0.26	5.62	10.17	3.00	0.19	0.33	0.02	98.40

Notes: In the Point column, the first number indicates the number of the circle drawn on the thin section, and the second number indicates the sequential number of analyses in that circle.

G = glass, P = palagonite, S = dark spherulitic glass.

Table T6. Composition of myrmekitic intergrowth and zeolite.

Core, section, interval (cm)	Point	Phase	Major element oxide (wt%)													
			SiO ₂	TiO ₂	Al ₂ O ₃	Cr ₂ O ₃	FeO	MnO	MgO	CaO	K ₂ O	Na ₂ O	BaO	P ₂ O ₅	Total	
200-1224D-																
3R-1, 14-16	1-7	Myrmekitic intergrowth	79.79	0.47	11.10	0.00	1.36	0.05	0.04	1.17	0.24	5.43	0.00	0.09	99.74	
	2-1	Myrmekitic intergrowth	78.40	0.48	11.67	0.04	1.26	0.00	0.06	1.01	0.33	6.03	0.00	0.05	99.33	
	2-2	Myrmekitic intergrowth	78.42	0.31	12.46	0.00	0.82	0.08	0.04	0.96	0.34	6.19	0.00	0.09	99.70	
200-1224F-																
6R-1, 29-34	2-2	Zeolite in pillow rim	63.99	0.09	20.49					0.04	4.34	6.76		0.02	95.73	

Note: In the Point column, the first number indicates the number of the circle drawn on the thin section, and the second number indicates the sequential number of analyses in that circle.